Vilniaus universiteto

Fizikos fakulteto

Cheminės fizikos institutas

Jakov Braver

Molekulinių sistemų fluorescencijos Štarko spektrų modeliavimas

Magistrantūros studijų baigiamasis darbas

Teorinės fizikos ir astrofizikos

studijų programa

Studentas	Jakov Braver
Leista ginti	2021-05-20
Darbo vadovas	doc. dr. Andrius Gelžinis
Instituto direktorius	prof. dr. (HP) Valdas Šablinskas

Vilnius 2021

Vilnius University

Faculty of Physics

Institute of Chemical Physics

Jakov Braver

Modelling of Stark Fluorescence Spectra of Molecular Systems

Master's final thesis

Theoretical Physics and Astrophysics

study programme

Student	Jakov Braver
Approved	2021-05-20
Academic supervisor	Assoc. Prof. Andrius Gelžinis
Director of the Institute	Prof. Valdas Šablinskas

Vilnius 2021

Contents

Introduction

Optical spectroscopy experiments are an essential tool for probing the properties of molecular systems [1]. Their complete characterisation requires determining a large number of parameters, and this, in turn, has stimulated the development of the broad variety of experimental techniques that are available today. An important class of experimental methods belongs to the domain of Stark spectroscopy, whereby the conventional absorption [2–4], fluorescence [5,6], or even two-dimensional spectroscopy [7] experiments are performed with an additionally applied external static electric field [8–10]. Specifically, the Stark fluorescence (and, similarly, absorption) spectrum is defined as the difference of two spectra: one registered with an externally applied electric field, and one without it. Such a setup allows one to determine the static dipole moments and polarisabilities of the system components. In particular, these experiments provide a way of identifying and parametrising the charge-transfer (CT) states. A CT state may form as an intermediate state of an excitation energy transfer reaction when an electron of an excited molecule (donor) becomes localised on another molecule (acceptor) [11]. The excitation energy transfer involving the CT states is essential for the early stages of photosynthesis [11,12], and the CT states seem to constitute an important part of the non-photochemical quenching mechanism [13].

Interpretation of experimental data, however, is no trivial task due to the interweaving of various effects that occur in real systems. To extract numerical values of parameters of interest, such as the dipole moments and polarisabilities, they have to be incorporated into a model, and a fit of the experimental data should be produced. If an agreement is obtained, then the used values can be considered correct. The first theoretical model that has been proposed for analysing the Stark spectroscopy data is due to Liptay [8] — it enables one to express the Stark fluorescence (absorption) spectrum as a linear combination of the zeroth, first, and the second derivatives of the corresponding field-free spectrum. By virtue of its simplicity and straightforward interpretation, this model has proven to be an effective tool for determining system parameters from the Stark spectra, and it continues to be the default method of analysis [5,6,13]. Nevertheless, some authors have questioned the applicability of this model because the parameters obtained from the fit were unphysical in certain cases [14]. It has been argued that the underlying assumptions may no longer be satisfied for systems such as molecular aggregates, where the excitonic levels may be arbitrarily close [15]. A new method for simulations of spectroscopic signals has been developed in Ref. [15], which, however, is only targeted at Stark absorption experiments. To the best of our knowledge, no attempts to simulate Stark fluorescence spectra using a microscopic theory have been made so far, and the present study is the first work in this direction.

The aim of this work is to simulate the Stark fluorescence spectra of model molecular systems and determine how the presence of CT states influences the shapes of the spectra. In the process, we check whether the Liptay formalism yields results consistent with those obtained using a numerically exact method. Additionally, we apply the quantum-classical theory to the calculations of the Stark fluorescence spectra to find whether such an approach could be used in cases when the system does not allow for a numerically exact treatment.

1 Methods

1.1 Definition of the model

In this work we will study the properties of a small molecular aggregate — a molecular dimer. We shall speak of a dimer as a pair of molecules (monomers) that are spatially well-separated and hence are bound non-covalently [16]. In this case the monomers interact electrostatically, and the interaction may be adequately described in the dipole approximation [11]. The chlorophyll ($\mathrm{Chl_{D1}}$) and the pheophytin ($\mathrm{Pheo_{D1}}$) molecules bound together in the Photosystem II reaction centre [12,16,17] are an example of such a dimer — the distance between them is about 10 Å, but their interaction plays an important role in the process of photosynthesis [2, 17, 18].

In order to simulate real spectroscopic experiments, it is necessary to consider the system of interest not as an isolated entity, but as one interacting with its surrounding environment, such as a solvent. Full quantum calculations of these composite systems are notoriously demanding in terms of required computational resources [19,20], and a different approach is required. In the recent years, it has been proven effective to apply the theory of open quantum systems [11, 21] to study such aggregates, to the extent that the results of the simulations may be directly compared with the experimental data [17, 22–25]. Therefore, this is the approach adopted in the present work.

Every application of the said theory begins with a separation of the total system to a small *subsystem* that is of main interest and its environment, termed the *bath*. The total Hamiltonian is written in its most general form as

$$\hat{H}_{\mathrm{T}} = \hat{H}_{\mathrm{S}} + \hat{H}_{\mathrm{B}} + \hat{H}_{\mathrm{SB}} + \hat{H}_{\mathrm{SF}} + \hat{H}_{\mathrm{F}}. \tag{1}$$

The terms $\hat{H}_{\mathrm{S}}$ and $\hat{H}_{\mathrm{B}}$ describe the subsystem and the bath, respectively, and their interaction is accounted for by the $\hat{H}_{\mathrm{SB}}$ term. Calculations of spectroscopic properties require an additional term, denoted $\hat{H}_{\mathrm{SF}}$ in the above formula, responsible for the interaction between the subsystem and the external electromagnetic field. If this field is treated quantum-mechanically (as in the present work), its Hamiltonian $\hat{H}_{\mathrm{F}}$ has to be included as well.

The first three Hamiltonians in Eq. (1) depend of the model of the system, and they are defined in the two following sections. The last two terms having a more general nature are defined while discussing the methods of calculations of fluorescence spectra in Section 1.2.

1.1.1 The electronic subsystem

As we are mostly interested in the emission spectrum of the dimer, our main focus is on the electronic transitions of the system. Consequently, we define our subsystem as the electronic degrees of freedom (DOFs) of the dimer. Each of its constituent monomers contributes its highest occupied molecular orbital (HOMO) and the lowest unoccupied molecular orbital (LUMO) to the total manifold of accessible states, also called *sites*. Two models that are widely used to further parametrise the subsystem are the Frenkel exciton model [16] and the more

recently developed tight-binding electron–hole model [26]. We will use the latter approach as it is better suited for describing the CT states by virtue of direct modelling of electrons and holes.

Let $|0\rangle$ denote the composite ground state whereby both monomers occupy their HOMOs (i.e., there are two electrons residing on the two HOMO orbitals of the system). We then define operators $\hat{e}_m^\dagger$ and $\hat{h}_m^\dagger$ that act on $|0\rangle$ creating, respectively, an electron on the LUMO and a hole on the HOMO of the m-th monomer. The possible singly-excited states are the molecular excitations,

$$|m^*\rangle \equiv \hat{e}_m^\dagger \hat{h}_m^\dagger |0\rangle \,, \tag{2}$$

and the CT states

$$\left|m^- n^+\right\rangle \equiv \hat{e}_m^\dagger \hat{h}_n^\dagger |0\rangle \,, \tag{3}$$

where the electron and the hole created as a result of an excitation occupy different monomers. Additionally introducing the corresponding annihilation operators $\hat{e}_m$ and $\hat{h}_m$ that fulfil the Fermi anticommutation relations, we may finally construct the subsystem Hamiltonian as [17]

$$\hat{H}_\mathrm{S} = \sum_{m,n} t_{mn}^e \hat{e}_m^\dagger \hat{e}_n + \sum_{m,n} t_{mn}^h \hat{h}_m^\dagger \hat{h}_n - \sum_{m,n} V_{mn}^{eh} \hat{e}_m^\dagger \hat{h}_n^\dagger \hat{h}_n \hat{e}_m + \sum_{m \neq n} J_{mn} \hat{e}_m^\dagger \hat{h}_m^\dagger \hat{h}_n \hat{e}_n. \tag{4}$$

Each index in the double sums runs over all excited electronic levels included in the problem, from 1 to N_el, except the last sum, where the terms $m \neq n$ are excluded. The terms $m \neq n$ in the first two sums represent the hopping of the electrons and holes between different monomers m and n, which may occur in an excited state. The corresponding hopping rates are denoted by t_{mn}^e and t_{mn}^h, while the diagonal terms t_{mm}^e and t_{mm}^h are the energies required to create, respectively, an electron and a hole on monomer m. Further, V_{mn}^{eh} is the Coulomb attraction energy between an electron on site m and a hole on site n, and J_{mn} is the 'resonance' Coulomb coupling between the monomers m and n corresponding to the dipole–dipole interaction. Since we restrict the analysis to the singly-excited states, we ignore the electron–electron and hole–hole repulsion energies; these become relevant only for multiply-excited states [17].

For a better understanding of the structure of Hamiltonian (4), let us analyse its matrix elements. The diagonal elements of $\hat{H}_\mathrm{S}$ in the *site basis* $\{|m^- n^+\rangle\}$ are[1]

$$\langle m^*| \hat{H}_\mathrm{S} |m^*\rangle \equiv \varepsilon_{m^*} = t_{mm}^e + t_{mm}^h - V_{mm}^{eh}, \tag{5}$$

$$\left\langle m^- n^+\right| \hat{H}_\mathrm{S} \left|m^- n^+\right\rangle \equiv \varepsilon_{m^- n^+} = t_{mm}^e + t_{nn}^h - V_{mn}^{eh}, \tag{6}$$

where we denote the energy of the excited state $|m\rangle^*$ by ε_{m^*} and the energy of the CT state $|m^- n^+\rangle$ by $\varepsilon_{m^- n^+}$. As we can see, the energies ε_{m^*} and $\varepsilon_{m^- n^+}$ needed to create an excited state consist of the energies required to create an electron (t_{mn}^e) and a hole (t_{mn}^h), and the electron–hole interaction energy V_{mn}^{eh} that plays the role of the binding energy. For the purposes of simulations, however, these constituent terms need not be specified.

[1] We use the identities $\hat{e}_m \hat{e}_n^\dagger |0\rangle = \hat{h}_m \hat{h}_n^\dagger |0\rangle = \delta_{mn} |0\rangle$.

The couplings between the different states of the site basis are given by

$$\langle m^*|\,\hat{H}_\mathrm{S}\,|n^*\rangle = J_{mn}, \tag{7}$$

$$\langle m^*|\,\hat{H}_\mathrm{S}\,\left|k^- l^+\right\rangle \equiv J_{m^*k^-l^+} = \delta_{ml}t^e_{mk} + \delta_{mk}t^h_{ml}, \tag{8}$$

$$\left\langle m^- n^+\right|\,\hat{H}_\mathrm{S}\,\left|k^- l^+\right\rangle = \delta_{nl}t^e_{mk} + \delta_{mk}t^h_{nl}. \tag{9}$$

The first equation confirms that parameters J_{mn} represent the coupling strength between two molecular excitations.[2] The couplings $J_{m^*k^-l^+}$ will be used directly rather than the hopping rates, while the couplings between two CT states will not be used altogether as we will include at most one CT state in the simulations.

In the rest of this work, we will use the simpler notation $|n\rangle$, where $n = 1, \ldots N_\mathrm{el}$, for both molecular excitations and CT states. The characters of the states will be states explicitly. Likewise, sums running from 1 to N_el will enumerate all subsystem states, both molecular excitations and CT states.

1.1.2 The vibrational bath

The remainder of the total system, which consists of the vibrational DOFs of the dimer and the environment, will constitute the bath. While the electronic subsystems has been specified in great detail, the bath will be treated more generically. It is sufficient to assume that each vibrational DOF may be adequately described as a normal-mode harmonic oscillator [11, 27] and that each electronic level has N_osc oscillators in its environment. Formally, we have

$$\hat{H}_\mathrm{B} = \sum_{n=1}^{N_\mathrm{el}} \sum_{\nu=1}^{N_\mathrm{osc}} \frac{\omega_{n\nu}}{2}(\hat{X}^2_{n\nu} + \hat{P}^2_{n\nu}), \tag{12}$$

where $\hat{X}_{n\nu}$ is the dimensionless coordinate operator of the ν-th oscillator coupled to the n-th state, $\hat{P}_{n\nu}$ is the corresponding momentum operator, and $\omega_{n\nu}$ is the frequency of the oscillator. Note that we use the relativistic units throughout this work: $\hbar = 1$, $c = 1$. The terms 'energy' and 'frequency' will therefore be used interchangeably, and these quantities will be measured in cm^{-1}.

The subsystem–bath interaction occurs through the coupling of bath modes to the excited states of subsystem. Therefore, the corresponding Hamiltonian is constructed as a (tensor)

[2] Alternatively, this can be seen by noticing that we may insert an operator $|0\rangle\langle 0|$ in the last sum in Eq. (4) without changing the matrix elements of $\hat{H}_\mathrm{S}$. The summand then assumes a more suggestive form,

$$J_{mn}\hat{e}^\dagger_m\hat{h}^\dagger_m\,|0\rangle\langle 0|\,\hat{h}_n\hat{e}_n = J_{mn}\,|m^*\rangle\langle n^*|\,. \tag{10}$$

The reason for the specific combinations of operators in the last two sums in Eq. (4) may thus be intuitively understood using the analogies

$$\hat{e}^\dagger_m\hat{h}^\dagger_m\hat{h}_n\hat{e}_n \Leftrightarrow |m^*\rangle\langle n^*|\,, \quad \hat{e}^\dagger_m\hat{h}^\dagger_n\hat{h}_n\hat{e}_m \Leftrightarrow \left|m^- n^+\right\rangle\left\langle m^- n^+\right|. \tag{11}$$

product of the vibrational coordinate operator and the 'molecular coupling operator' [17]

$$\hat{H}_{\mathrm{SB}} = -\sum_{n=1}^{N_{\mathrm{el}}} \sum_{\nu=1}^{N_{\mathrm{osc}}} \omega_{n\nu} d_{n\nu} \hat{X}_{n\nu} \left|n\right\rangle\left\langle n\right| . \tag{13}$$

Interaction with the subsystem causes shifts in the average coordinates of bath oscillators, and the shift of the ν-th oscillator that interacts with the n-th excited state is denoted by $d_{n\nu}$. In practice, these parameters control the strength of interaction between the excited subsystem states and the bath oscillators.

The chosen system–bath interaction has the structural form

$$\hat{H}_{\mathrm{SB}} = \sum_{n} \hat{S}_n \hat{B}_n, \tag{14}$$

where $\hat{S}_n$ is a subsystem operator and $\hat{B}_n$ is a bath operator. In this case, the effects that the bath has on the subsystem are encoded in the *bath correlation function* [11, 27]

$$C_{mn}(t) = \mathrm{Tr}\Big(\hat{\rho}_{\mathrm{B}}^{\mathrm{eq}} \mathrm{e}^{\mathrm{i}\hat{H}_{\mathrm{B}}t} \hat{B}_m \mathrm{e}^{-\mathrm{i}\hat{H}_{\mathrm{B}}t} \hat{B}_n\Big) - \mathrm{Tr}(\hat{\rho}_{\mathrm{B}}^{\mathrm{eq}} \hat{B}_m)\mathrm{Tr}(\hat{\rho}_{\mathrm{B}}^{\mathrm{eq}} \hat{B}_n). \tag{15}$$

Here, $\hat{\rho}_{\mathrm{B}}^{\mathrm{eq}}$ is the bath equilibrium density operator given by the canonical distribution

$$\hat{\rho}_{\mathrm{B}}^{\mathrm{eq}} = \frac{\mathrm{e}^{-\beta\hat{H}_{\mathrm{B}}}}{\mathrm{Tr}(\mathrm{e}^{-\beta\hat{H}_{\mathrm{B}}})}, \tag{16}$$

where $\beta = k_{\mathrm{B}}T$, and k_{B} is the Boltzmann constant. For the chosen form of the Hamiltonian (13), the bath operators are just the sums of the coordinate operators,

$$\hat{B}_n = -\sum_{\nu=1}^{N_{\mathrm{osc}}} \omega_{n\nu} d_{n\nu} \hat{X}_{n\nu}, \tag{17}$$

and the correlation function (15) may be calculated explicitly[3] [11]. Analysis of its Fourier image, $C_{mn}(\omega)$, reveals that its odd and even parts contain the same information, and it is more convenient to work with the odd part $C''_{mn}(\omega)$ only, which is called the *spectral density* [11, 27]. In the present work, we assume that the different states m and n are uncorrelated; the corresponding spectral density $C''_n(\omega) \equiv \delta_{mn} C''_{mn}(\omega)$ of the harmonic oscillator bath is [11]

$$C''_n(\omega) = \frac{\pi}{2} \sum_{\nu=1}^{N_{\mathrm{osc}}} \omega_{n\nu}^2 d_{n\nu}^2 \Big(\delta(\omega - \omega_{n\nu}) - \delta(\omega + \omega_{n\nu})\Big), \tag{18}$$

where $\delta(\omega)$ is the Dirac delta-function. The spectral densities of molecular systems may be measured experimentally, and the results imply that it is reasonable to model them by well-defined continuous functions instead of the sums of the delta-functions [11]. To facilitate comparison of the results obtained with different methods (see Section 2), in our simulations we used the

[3] Note that $\mathrm{Tr}(\hat{\rho}_{\mathrm{B}}^{\mathrm{eq}} \hat{X}_{n\nu}) = 0$, so the second term in Eq. (15) vanishes.

Debye spectral density [11, 27]

$$C_n''(\omega) = \frac{2\lambda_n \gamma \omega}{\omega^2 + \gamma^2}. \tag{19}$$

Here, γ is the bath relaxation rate, and λ_n is the reorganisation energy that controls the strength of interaction between the bath and the n-th subsystem state. To see how λ_n are connected to the parameters $d_{n\nu}$, we may express the reorganisation energy as an integral over the spectral density and substitute its expression from Eq. (18):

$$\lambda_n = \frac{1}{\pi} \int_0^\infty \frac{C_n''(\omega)}{\omega} \, \mathrm{d}\omega = \sum_{\nu=1}^{N_{\mathrm{osc}}} \frac{\omega_{n\nu} d_{n\nu}^2}{2}. \tag{20}$$

Thus, having chosen the overall subsystem–bath interaction strength λ_n, we may calculate the strengths of interaction $d_{n\nu}$ between each n-th excitation and ν-th bath oscillator. To do so, we view the spectral density (18) as a discrete function of N_{osc} frequencies $\omega_{n\nu}$, so that

$$\tilde{d}_{n\nu} = \sqrt{\frac{2C_n''(\omega_{n\nu})}{\pi \omega_{n\nu}^2}}, \tag{21}$$

where $\tilde{d}_{n\nu}$ are the coupling strengths that can be readily calculated using the chosen form of the spectral density, Eq. (19) in our case. Such a choice, however, does not ensure that the normalisation condition (20) holds for the couplings $\tilde{d}_{n\nu}$. We have

$$\sum_{\nu=1}^{N_{\mathrm{osc}}} \frac{\omega_{n\nu} \tilde{d}_{n\nu}^2}{2} = A_n \implies \frac{\lambda_n}{A_n} \sum_{\nu=1}^{N_{\mathrm{osc}}} \frac{\omega_{n\nu} \tilde{d}_{n\nu}^2}{2} = \lambda_n, \tag{22}$$

where A_n is some constant that we can calculate. Comparing the implied equation with Eq. (20), the formula for the actual coupling strengths $d_{n\nu}$ follows as

$$d_{n\nu} = \sqrt{\frac{\lambda_n}{A_n}} \tilde{d}_{n\nu}. \tag{23}$$

1.2 Calculations of fluorescence spectra

In this section, we discuss the methods of calculation of stationary (or relaxed) fluorescence spectra of molecular systems in the absence of any external electromagnetic fields. The static external field present in the Stark spectroscopy experiments will be treated in the next section. Let us first state the assumptions about the physical experiment that we seek to simulate.

The molecular subsystem is assumed to be excited by an infinitely short laser pulse, and subsequent 'equilibration' — relaxation to the lowest (i.e., singly excited) electronic levels of the excited electronic state manifold — is assumed to be instantaneous as well. Therefore, we do not take into account any photons emitted during the equilibration period, but rather restrict the analysis to the photons emitted thereafter. Since radiative lifetime of the molecular excited states is often on the order of nanoseconds and the equilibration time of the excited

states is a few to tens of picoseconds [11], our assumption of instantaneous excitation and the following equilibration corresponds to this separation of timescales. Finally, we ignore the multi-photon relaxation and any nonradiative relaxation channels, such as thermal decay or internal conversion [11].

The fluorescence spectrum $f(\omega, t)$ of a molecular system is effectively a distribution function of photon frequencies which shows the number of photons per unit frequency range (around ω) that the system emits per unit time at time t after excitation. We aim at describing the relaxed fluorescence spectrum, therefore we are interested in the steady-state distribution $f(\omega)$. It may be conveniently calculated as a sum of single-mode distributions $f_{\boldsymbol{k}s}(t)$ that describe emission of photons with frequencies corresponding to a specific wave vector $|\boldsymbol{k}| = \omega_{\boldsymbol{k}}$ and a specific polarisation s.

From a purely quantum perspective, the rate of emission of a photon with a wave vector $\boldsymbol{k}$ and polarization s may be calculated as the rate of change of the occupation number corresponding to the $(\boldsymbol{k}, s)$ mode of the electromagnetic wave [27, 28]. The occupation number operator is given by

$$\hat{\mathcal{N}}_{\boldsymbol{k}s} = \hat{a}^\dagger_{\boldsymbol{k}s}\hat{a}_{\boldsymbol{k}s}, \tag{24}$$

where operators $\hat{a}_{\boldsymbol{k}s}$ and $\hat{a}^\dagger_{\boldsymbol{k}s}$ are the bosonic photon annihilation and creation operators. We must now find the operator $\hat{f}_{\boldsymbol{k}s}$ that corresponds to the emission rate observable $f_{\boldsymbol{k}s}$. By identifying the photon emission rate with the emission spectrum [27], we adopt one of the several possible quantum definitions of the spectrum [29]. Such an intuitive definition turns out to be adequate for the present analysis as the spectra calculated using the final formula agree with the measured spectra reasonably well [22, 24].

It follows from our definition of the emission rate that

$$f_{\boldsymbol{k}s}(t) = \frac{\mathrm{d}}{\mathrm{d}t}\mathcal{N}_{\boldsymbol{k}s}(t), \tag{25}$$

where $\mathcal{N}_{\boldsymbol{k}s}$ is the mode occupation number observable which operator $\hat{\mathcal{N}}_{\boldsymbol{k}s}$ corresponds to. The operator $\hat{f}_{\boldsymbol{k}s}$ corresponding to the time derivative of $\mathcal{N}_{\boldsymbol{k}s}$ is then given by [30]

$$\hat{f}_{\boldsymbol{k}s} = \mathrm{i}[\hat{H}_\mathrm{T}, \hat{\mathcal{N}}_{\boldsymbol{k}s}], \tag{26}$$

where $\hat{H}_\mathrm{T}$ is the total Hamiltonian of the composite system. At this point, the forms of the last two Hamiltonians in Eq. (1) become relevant. The free-field Hamiltonian of the electromagnetic field is given by [28, 31, 32]

$$\hat{H}_\mathrm{F} = \sum_{\boldsymbol{k},s} \omega_{\boldsymbol{k}} \left(\hat{a}^\dagger_{\boldsymbol{k}s}\hat{a}_{\boldsymbol{k}s} + \frac{1}{2} \right), \tag{27}$$

while the system–field interaction Hamiltonian is taken to be of the form

$$\hat{H}_\mathrm{SF} = -\hat{\boldsymbol{\mu}} \cdot \hat{\boldsymbol{E}} = -\sum_{n=1}^{N_\mathrm{el}} \boldsymbol{\mu}_{0n}(\hat{e}^\dagger_n \hat{h}^\dagger_n + \hat{e}_n \hat{h}_n) \cdot \hat{\boldsymbol{E}} \tag{28}$$

where $\hat{\boldsymbol{\mu}}$ is the dipole moment operator, $\boldsymbol{\mu}_{0n}$ is the transition moment from state $|n^*\rangle$ to the ground state, and $\hat{\boldsymbol{E}}$ is the standard second-quantised electric field strength operator [28,31,32]. Note that here we ignore the diagonal elements of $\hat{\boldsymbol{\mu}}$ that become relevant only when an external electric field is applied. This Hamiltonian corresponds to the dipole approximation [27, 28], whereby it is assumed that each molecule may be adequately described as a single electric dipole, neglecting higher order effects related to the magnetic dipole moment and electric quadrupole moment. Therefore, the electric field is assumed not to change appreciably over the dimensions of the molecules. This approximation is valid as long as the wavelength of the radiation is much greater than the size of the molecule. For example, the dimensions of a porphyrin ring of a chlorophyll molecule are $\lesssim 1\,\mathrm{nm}$, clearly much less than the wavelength of visible light.

The aim is now to find the quantum average of the emission rate operator (26). We approach it with the help of the density matrix formalism, which is mandatory when working with open quantum systems. Introducing the total density operator $\hat{\rho}_{\mathrm{T}}(t)$ that describes both the system and the field, we have

$$f_{\boldsymbol{ks}}(t) = \mathrm{Tr}_{\mathrm{T}}\Big(\hat{f}_{\boldsymbol{ks}}\hat{\rho}_{\mathrm{T}}(t)\Big) = \mathrm{Tr}_{\mathrm{T}}\Big(\mathrm{i}[\hat{H}_{\mathrm{T}}, \hat{\mathcal{N}}_{\boldsymbol{ks}}]\hat{\rho}_{\mathrm{T}}(t)\Big)\,, \tag{29}$$

where the index 'T' (total) emphasises that the trace is taken with respect to both the system and the field states. To proceed, we assume that the electromagnetic field is in the vacuum state initially (at some $t = 0$ when the system has reached excited state equilibrium and the fluorescence starts), so that only spontaneous emission, but not stimulated one, takes place. Further, the system–field interaction is assumed to act as a small perturbation, allowing one to use a perturbational expansion of the density matrix with respect to the electric field strength [27]. The next step is then to insert the first order solution of the Liouville–von Neumann equation

$$\frac{\mathrm{d}}{\mathrm{d}t}\hat{\rho}_{\mathrm{T}}(t) = -\mathrm{i}[\hat{H}_{\mathrm{T}}, \hat{\rho}_{\mathrm{T}}(t)] \tag{30}$$

into Eq. (29). After numerous manipulations, shown at full length in our previous work [33], we find that the spectrum may be obtained by calculating the dipole–dipole correlation function

$$C_{\mathrm{d-d}}(t) = \mathrm{Tr}_{\mathrm{SB}}\Big(\Big(\hat{\boldsymbol{\mu}}^{\mathrm{I}}(t)\cdot\boldsymbol{\sigma}_E\Big)\Big(\hat{\boldsymbol{\mu}}^{\mathrm{I}}(0)\cdot\boldsymbol{\sigma}_E\Big)\hat{\rho}_{\mathrm{SB}}(0)\Big) \tag{31}$$

and taking its Fourier transform:

$$f\left(\omega\right) \propto \omega^3 \Re \int_0^\infty \mathrm{d}t\ \left\langle C_{\mathrm{d-d}}(t)\right\rangle_{\mathrm{or}} \mathrm{e}^{-\mathrm{i}\omega t}, \tag{32}$$

where $\hat{\boldsymbol{\mu}}^{\mathrm{I}}(t)$ denotes the dipole moment operator in the interaction picture,

$$\hat{\boldsymbol{\mu}}^{\mathrm{I}}(t) = \mathrm{e}^{\mathrm{i}(\hat{H}_{\mathrm{S}}+\hat{H}_{\mathrm{SB}})t}\hat{\boldsymbol{\mu}}\mathrm{e}^{-\mathrm{i}(\hat{H}_{\mathrm{S}}+\hat{H}_{\mathrm{SB}})t}. \tag{33}$$

In an actual fluorescence experiment, usually the emitted light of a specific polarisation is

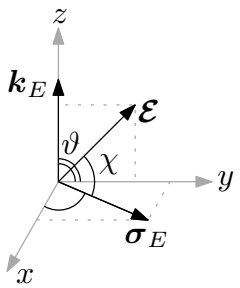

Figure 1: The geometry of the simulated experiment.

registered [34]; this unit polarisation vector is denoted by $\boldsymbol{\sigma}_E$ in Eq. (32). Also, it is important to account for the fact that the dipole moments of the molecules in the sample may be randomly oriented with respect to $\boldsymbol{\sigma}_E$. Therefore, an orientational averaging over all possible mutual orientations of $\boldsymbol{\sigma}_E$ and $\hat{\boldsymbol{\mu}}$ has to be performed, which is denoted by $\langle \bullet \rangle_{\text{or}}$ in Eq. (32). The specific details about the orientational averaging are given below.

The dipole moments of the molecules are most naturally specified in the molecular reference frames attached to each molecule of the sample. Meanwhile, the vector of polarisation that corresponds to a specific experimental setup has to be defined in a certain 'Lab' frame. Then, it is assumed that the dipole moment vectors are the same in all molecular reference frames, but these frames are randomly oriented with respect to the Lab frame. Denoting the Euler angles [35] between the molecular and Lab frames by α, β, and γ, the orientational averaging may be expressed as [34]

$$\langle g(\alpha,\beta,\gamma)\rangle_{\text{or}} = \frac{1}{8\pi^2}\int\limits_0^{\pi}\int\limits_0^{2\pi}\int\limits_0^{2\pi} g(\alpha,\beta,\gamma)\sin\alpha\,\mathrm{d}\alpha\,\mathrm{d}\beta\,\mathrm{d}\gamma, \tag{34}$$

where $g(\alpha,\beta,\gamma)$ is an arbitrary function. In order to calculate the scalar products of vectors $\hat{\boldsymbol{\mu}}$ and $\boldsymbol{\sigma}_E$ defined in different reference frames, we transform the dipole moment operator to the Lab frame using the standard transformation matrix [34].

The geometry of the simulated experiment is shown in Fig. 1. The unit vector $\boldsymbol{k}_E$ shows the direction of propagation of the light that is registered, and $\boldsymbol{\sigma}_E$ defines the corresponding polarisation. The vector $\boldsymbol{\mathcal{E}}$ shows the direction of the static external electric field relevant for the Stark fluorescence experiments. We used a typical choice [2] of the angles shown in the figure: $\vartheta = \pi/4$ and $\chi = \varphi_{\text{magic}}$ with $\cos\varphi_{\text{magic}} = 1/\sqrt{3}$.

Now let us consider the operator $\hat{\rho}_{\text{SB}}(0) \equiv \text{Tr}_{\text{F}}\big(\hat{\rho}_{\text{T}}(0)\big)$ under the trace of Eq. (32). This term stands for the excited state equilibrium density matrix of the system (subsystem + bath), with the electromagnetic field DOFs traced out. In order to calculate $\hat{\rho}_{\text{SB}}(0)$, we assume that the subsystem and the bath are uncorrelated in the beginning of the experiment (at $t = t_0 < 0$), which means that the density operator of the system may be written as a (tensor) product of the density operators of the subsystem and the bath,

$$\hat{\rho}_{\text{SB}}(t_0) = \hat{\rho}_{\text{S}}(t_0)\hat{\rho}_{\text{B}}(t_0). \tag{35}$$

Here, the subsystem is taken to occupy the ground state, $\hat{\rho}_{\mathrm{S}}(t_0) = |0\rangle\langle 0|$, while the bath is in thermal equilibrium, $\hat{\rho}_{\mathrm{B}}(t_0) = \hat{\rho}_{\mathrm{B}}^{\mathrm{eq}}$, as given by Eq. (16). At this point, the subsystem is excited (by a laser pulse), causing the subsystem and the bath to interact until a new equilibrium state is reached. Note that this state is different from the initial one, as the subsystem reaches a certain superposition of the excited states rather than the ground state. The bath also adapts accordingly and evolves to a state different from $\hat{\rho}_{\mathrm{B}}^{\mathrm{eq}}$. From the perspective of simulations, we therefore have to calculate the dynamics of the relaxation process using the initial condition (35). Once the system has equilibrated, we 'open' the optical relaxation channel[4] and calculate the relaxation dynamics. Specifically, we calculate the evolution of $\hat{\boldsymbol{\mu}}(t)$ until the dipole–dipole correlation function (31) has decayed to zero (to a given tolerance). Having obtained the operator $\hat{\boldsymbol{\mu}}(t)$ at discrete time points, we calculate $C_{\mathrm{d-d}}(t)$ and take its Fourier transform to obtain the final spectrum.

When the spectra are simulated numerically, one is usually only interested in the shape of the spectrum rather than its absolute magnitude. Indeed, the shape contains all the available information about the system, and the spectrum always has to be normalised to match the experimental data. For this reason, the dimensional constants are omitted in Eq. (32). To be specific, we will associate with a spectrum the following quantity:

$$F(\omega) = \Re \int_{-\infty}^{\infty} \mathrm{d}t\, \Theta(t)\, \langle C_{\mathrm{d-d}}(t)\rangle_{\mathrm{or}}\, \mathrm{e}^{-\mathrm{i}\omega t}. \tag{36}$$

Here, as is customary when working with spectra of model systems [25,36,37], we omitted the factor of ω^3 which does not make any noticeable difference because the spectrum is non-zero only in a small interval of ω. We have also introduced a function $\Theta(t)$ defined to be equal to 0 for $t < 0$ and 1 for $t \geq 0$. Having written the function $F(\omega)$ in such a form, we may easily obtain an expression for the integral of $F(\omega)$ which will be important for the analysis of the spectra. Integrating both sides of Eq. (36) over all frequencies, we obtain

$$\int_{-\infty}^{\infty} \mathrm{d}\omega\, F(\omega) = 2\pi\, \langle C_{\mathrm{d-d}}(0)\rangle_{\mathrm{or}}\,. \tag{37}$$

Here, we assume that $C_{\mathrm{d-d}}(0)$ is real, which holds true if $\hat{\boldsymbol{\mu}}$ is real (see Eq. (31); the equilibrium density operator $\hat{\rho}_{\mathrm{SB}}(0)$ is necessarily real).

An additional remark regarding Eq. (36) is in order. It is important to recognise that $f(\omega)$ from Eq. (32), and hence also $F(\omega)$, is the *rate* of emission of photons, while in an actual experiment, the *total number* of emitted photons of each frequency, $S(\omega)$, is registered. However, as $F(\omega)$ is constant (in time), we have simply $S(\omega) = \tau F(\omega)$, where τ is the duration of observation. Therefore, the function $S(\omega)$ measured in an experiment is directly proportional to $F(\omega)$ that we may calculate using Eq. (36), and the shapes of these two functions are the

[4] As mentioned in the beginning of this section, the electronic relaxation process is a few orders of magnitude faster than the optical relaxation, so it is physically justified to assume that fluorescence starts only after the relaxed state is reached.

same. This holds even if we take into account that the emission rate will eventually fall down to zero due to the reduction of populations with time[5]. In this case, the actual emission rate is $F(\omega)u(t)$, where $u(t)$ is some decaying function, such as e^{-t}, but we again have $S(\omega) = \int_0^\infty \mathrm{d}t\, F(\omega)u(t) \propto F(\omega)$. This justifies our identification of $F(\omega)$ with the spectrum that may be obtained experimentally.

1.3 Stark fluorescence spectra

The Stark fluorescence spectrum is defined as the difference of two spectra [9, 10]:

$$F_{\mathrm{S}}(\omega) = F_{\mathcal{E}}(\omega) - F(\omega), \tag{38}$$

where $F_{\mathcal{E}}(\omega)$ is the fluorescence spectrum in the presence of an external static electric field of strength $\boldsymbol{\mathcal{E}}$, while $F(\omega)$ is the fluorescence spectrum when no external field is applied. Let us review the main effects that cause the differences in these two spectra.

If the system possesses a static dipole moment $\boldsymbol{\mu}'_{nn}$ in a certain state $|n\rangle$, the energy ε_n of that state will shift if an external electric field is applied:

$$\varepsilon'_n = \varepsilon_n - \boldsymbol{\mu}'_{nn} \cdot \boldsymbol{\mathcal{E}}. \tag{39}$$

This is the essence of the Stark effect which causes line splitting in the atomic spectra and band broadening in the spectra of molecular systems [38]. In the general case, not only the energies of the states but also the directions and the magnitudes of all dipole moments of the system may change in an external field [39]:[6]

$$\boldsymbol{\mu}'_{mn} = \boldsymbol{\mu}_{mn} + \hat{\alpha}_{mn}\boldsymbol{\mathcal{E}} + \mathcal{O}(\boldsymbol{\mathcal{E}}^2). \tag{40}$$

Here, $\boldsymbol{\mu}_{mn}$ are the matrix elements of the dipole moment operator already encountered in Eq. (28); its diagonal elements are the *static* dipole moments, while the off-diagonal ones are the *transition* dipole moments. The term $\hat{\alpha}_{mn}$ is the polarisability tensor describing the field-induced change of the mn-th dipole moment. For further analysis of the spectra, it is convenient to define the differences between the static dipole moments in the excited states and the ground state:

$$\Delta\boldsymbol{\mu}_{nn} = \boldsymbol{\mu}_{nn} - \boldsymbol{\mu}_{00}. \tag{41}$$

Assuming we are dealing with a sample of randomly oriented molecules, it is clear from Eq. (39) that the energy shifts will not be the same for all molecules since the shift depends on the mutual orientations of $\boldsymbol{\mu}'_{nn}$ and $\boldsymbol{\mathcal{E}}$. The energy levels will effectively split, causing broader spectral bands of $F_{\mathcal{E}}(\omega)$ compared with those of $F(\omega)$. Moreover, the intensities of the maxima of the spectral bands will reduce, similarly to the reduction of intensity of spectral lines in the case of atomic Stark effect. Further, as long as the field-induced change in the dipole

[5] This is caused by the radiative relaxation and also by nonradiative relaxation channels.

[6] Equation (40) is given in the Gaussian units.

moment is negligible, $|\hat{\alpha}_{mn}\boldsymbol{\mathcal{E}}| \ll |\boldsymbol{\mu}_{mn}|$, the positions of the maxima of the bands will not exhibit a shift since the broadening will be symmetrical around ε_n. The said requirement is in fact satisfied for most realistic molecules and field strengths used in experiments, with the typical ratio being $|\hat{\alpha}_{mn}\boldsymbol{\mathcal{E}}|/|\boldsymbol{\mu}_{mn}| \sim 10^{-3}$ [8]. Finally, if the molecules are not isolated and are in thermal contact with an environment (such as a solvent), orientational effects may arise. Based on thermodynamical considerations, it will be energetically more favourable for molecules to rotate in such a way so as minimise their energy. Specifically, if the molecules are in thermal equilibrium with the environment and each molecule is in a certain state $|n\rangle$, then the probability that the angle between vectors $\boldsymbol{\mu}_{nn}$ and $\boldsymbol{\mathcal{E}}$ equals ϑ is given by the Boltzmann factor [39]:

$$p_n(\vartheta) \propto \exp\left(-\frac{\varepsilon_n - \boldsymbol{\mu}_{nn}\cdot\boldsymbol{\mathcal{E}}}{k_{\mathrm{B}}T}\right) \propto \exp\left(\frac{\mu_{nn}\mathcal{E}\cos\vartheta}{k_{\mathrm{B}}T}\right). \tag{42}$$

As a result, the intensity of the spectral bands of $F(\omega)$ may either increase or decrease, and an overall redshift of $F_{\mathcal{E}}(\omega)$ with respect to $F(\omega)$ may be observed [39]. These effect are, however, also rather minute: the relative change of intensity of the spectral bands of $F(\omega)$ is $\sim 10^{-4}$, and the shift of the spectral bands makes up only $\sim 10^{-3}$ of the full width at half maximum of the bands [39].

An experimentally obtained Stark spectrum contains contributions from all of the above effects, so that extracting system parameters becomes problematic. The first model that was proposed to analyse the Stark spectra is due to Liptay, and it lets one express the Stark fluorescence spectrum as a sum of derivatives of the corresponding field-free fluorescence spectrum [8, 10]:[7]

$$F_{\mathrm{S}}(\omega) = \mathcal{E}^2\left(A_\chi F(\omega) + \frac{B_\chi}{15}\frac{\mathrm{d}}{\mathrm{d}\omega}F(\omega) + \frac{C_\chi}{30}\frac{\mathrm{d}^2}{\mathrm{d}\omega^2}F(\omega)\right). \tag{43}$$

This formula is obtained assuming that the fluorescing molecules are immobilised and that the change of intensity and position of the spectral bands when the field is applied is relatively small [8, 10]. The first two terms describe the dependence of the fluorescence spectrum on the polarisabilities and hyperpolarisabilities of the dipole moments, while the last term encompasses contributions from the differences of the static dipole moment ($\Delta\boldsymbol{\mu}_{nn}$). We will not be concerned with the effects caused by the polarisabilities, so the exact expressions for the coefficients A_χ and B_χ will not be important. If we set $A_\chi = B_\chi = 0$, then the Stark spectrum is given only by the second derivative of the fluorescence spectrum, and the corresponding weighting coefficient is [9, 10]

$$C_\chi^n = |\Delta\boldsymbol{\mu}_{nn}|^2\Big(5 + (3\cos^2\chi - 1)(3\cos^2\zeta - 1)\Big). \tag{44}$$

The formula (43) should be used for each spectral band separately, so the coefficient given in Eq. (44) actually describes the band corresponding to the transition $|n\rangle \to |0\rangle$. The symbol χ denotes the angle between $\boldsymbol{\mathcal{E}}$ and $\boldsymbol{\sigma}_E$ (see Fig. 1), and ζ is the angle between $\boldsymbol{\mu}_{0n}$ and $\Delta\boldsymbol{\mu}_{nn}$. Note

[7] Note that we operate with the quantity $F(\omega)$ defined in Eq. (36) that does not have the ω^3 factor originally present in Eq. (32). Therefore, contrary to the usual form of Eq. (43) (see, e.g., Refs. [8–10]) we may write simply $\frac{\mathrm{d}}{\mathrm{d}\omega}F$ instead of $\omega^3\frac{\mathrm{d}}{\mathrm{d}\omega}\frac{F}{\omega^3}$, and $\frac{\mathrm{d}^2}{\mathrm{d}\omega^2}F$ instead of $\omega^3\frac{\mathrm{d}^2}{\mathrm{d}\omega^2}\frac{F}{\omega^3}$.

that by choosing the former angle so that $\cos^2\chi = 1/3$, the coefficient C_χ^n becomes independent of the angle ζ. This allows one to determine the parameter $|\Delta\boldsymbol{\mu}_{nn}|^2$ directly from the fit of experimental data.

Our simulations of the Stark fluorescence spectra have been performed using the definition (38): two spectra, with and without an external field, were simulated and their difference was taken. The formalism laid out in the previous section remains largely the same when an external field is included, but a few notable differences have to be considered. When an external electric field is present, it is no longer reasonable to assume that the electromagnetic field is in the vacuum state. In this case, it is most convenient to model the initial state of the field in terms of *coherent states* [32, 40, 41]:

$$\hat{\rho}_{\mathrm{F}}(0) = |\{z_{\boldsymbol{k}s}\}\rangle\langle\{z_{\boldsymbol{k}s}\}|\,, \tag{45}$$

where notation $|\{z_{\boldsymbol{k}s}\}\rangle$ means that each mode of the field is in a coherent state, defined as the eigenvector of the photon annihilation operator:

$$\hat{a}_{\boldsymbol{k}s}\,|z_{\boldsymbol{k}s}\rangle = z_{\boldsymbol{k}s}\,|z_{\boldsymbol{k}s}\rangle\,. \tag{46}$$

Using these states, it is possible to find an explicit expression for the field state wherein the expectation value of the electric field strength operator matches the required classical value, $\boldsymbol{\mathcal{E}}$ in our case [40]. Then, we should repeat the derivation [33] of the formula (36) for the spectrum, with the subsystem–field interaction given by Eq. (28), but the initial density matrix of the field being in the form (45). However, a simpler approach is possible. Using the properties of coherent states, the Liouville equation (30) maybe transformed in such a way so that the subsystem–field interaction Hamiltonian part of $\hat{H}_{\mathrm{T}}$ becomes [42]

$$\hat{H}_{\mathrm{SF}} = -\hat{\boldsymbol{\mu}}\cdot(\hat{\boldsymbol{E}} + \boldsymbol{\mathcal{E}}), \tag{47}$$

and the initial condition for the field is now the vacuum state. Thus, the final formula (36) remains valid in the presence of an external electric field at the expense of an additional term $(-\hat{\boldsymbol{\mu}}\cdot\boldsymbol{\mathcal{E}})$ now appearing when transforming $\hat{\boldsymbol{\mu}}$ to the interaction picture:

$$\hat{\boldsymbol{\mu}}^{\mathrm{I}}(t) = \mathrm{e}^{\mathrm{i}(\hat{H}_{\mathrm{S}}+\hat{H}_{\mathrm{SB}}-\hat{\boldsymbol{\mu}}\cdot\boldsymbol{\mathcal{E}})t}\,\hat{\boldsymbol{\mu}}\,\mathrm{e}^{-\mathrm{i}(\hat{H}_{\mathrm{S}}+\hat{H}_{\mathrm{SB}}-\hat{\boldsymbol{\mu}}\cdot\boldsymbol{\mathcal{E}})t}. \tag{48}$$

Note that when calculating the field-free spectra, only the off-diagonal elements of $\hat{\boldsymbol{\mu}}$ play a role (see Eq. (28)), but for the calculation of Stark spectra, the diagonal elements are essential. Also note that we adopt the convention that the diagonal elements of $\hat{\boldsymbol{\mu}}$ are the difference moments $\Delta\boldsymbol{\mu}_{nn}$ defined in Eq. (41).

1.4 The quantum-classical formalism

An important aspect of the fluorescence spectrum formula (36) is the orientational averaging. It can be calculated analytically if no external field is present since in that case one simply has to calculate the orientational average of $(\hat{\boldsymbol{\mu}} \cdot \boldsymbol{\sigma}_E)^2$, which results in a factor of 1/3 (see Ref. [34]). However, the analysis is complicated in the presence of the external field. Since it causes an orientation-dependent shift of energy levels (39), the equilibrium density matrix $\hat{\rho}_{\mathrm{SB}}(0)$ becomes dependent on the orientation as well. Analytical calculation of the average would only be possible if one had an explicit expression for $\hat{\rho}_{\mathrm{SB}}(0)$, which is not achievable for systems with many DOFs. Moreover, an explicit expression for $\hat{\boldsymbol{\mu}}^{\mathrm{I}}(t)$ would also be needed since the evolution of this operator depends on the orientation between $\hat{\boldsymbol{\mu}}$ and $\boldsymbol{\mathcal{E}}$ (see Eq. (48)). Thus, it only seems possible to perform the averaging by repeating calculations of the correlation function (31) with different orientations and calculating the mean. This operation induces substantial computational cost for methods conventionally used for calculating fluorescence spectra, such as the Hierarchical Equations Of Motion (HEOM) approach [36] or methods based on the Quantum Master Equation [22, 43]. A way to circumvent this issue is to apply a method of calculating system dynamics which is based on the Monte Carlo (MC) integration at its core. For such a method, three additional integration dimensions corresponding to the three Euler angles will not require any additional computational resources.

The MC integration method used in the present work is based on an approximate solution to the quantum-classical Liouville equation. This section is therefore devoted to introducing the underlying quantum-classical theory.

1.4.1 Quantum-classical Liouville equation

Any theory of open quantum systems must inevitably resort to approximations if the number of bath DOFs is large, and it seems reasonable to try applying classical mechanics for the description of the bath. For molecular simulations, this is justified if the subsystem in question corresponds to electronic DOFs, and the bath comprises nuclear DOFs. However, combining classical description of well-defined trajectories of coordinates and momenta of bath particles with the discrete Hilbert space of the subsystem requires some ingenuity. This may be accomplished by performing the Wigner transformation [11, 44, 45] which is defined for any operator $\hat{A}$ as[8]

$$A^{\mathrm{W}}(Q,P) = \int_{-\infty}^{\infty} \mathrm{d}Z\, \mathrm{e}^{\mathrm{i}PZ/\hbar} \left\langle Q - Z/2 \right| \hat{A} \left| Q + Z/2 \right\rangle . \tag{49}$$

To compute the transform, one has to start with the operator in the coordinate representation, $\hat{A}(X, X')$, and introduce 'new' coordinates $Q = (X + X')/2$ and $Z = X - X'$. Calculation of the integral then amounts to performing the Fourier transformation where the transformation parameter P is the momentum. The result, $A^{\mathrm{W}}(Q, P)$, is just a classical coordinate–momentum phase space distribution function. This interpretation, however, should not be taken too liter-

[8] In this section, ordinary units are used, and the Planck's constant $\hbar$ is restored.

ally because it is fundamentally impossible to determine the simultaneous probability of the coordinates and momenta of a quantum system. Formally, the definition (49) does not guarantee that $A^{\mathrm{W}}(Q,P)$ is everywhere positive, but it is necessarily real as long as $\hat{A}$ is Hermitian.

The next step in combining quantum and classical description in a single framework is to realise that we may perform a *partial* Wigner transformation, transforming only those DOFs which we wish to take into account approximately. In the present case we will want to transform all operators with respect to the bath coordinates — the resulting quantity will therefore remain an operator in the subsystem Hilbert space, while the Hilbert space of the bath will be reduced to a classical phase space.

The central equation of the quantum–classical formalism is obtained by performing a partial Wigner transformation of the Liouville–von Neumann equation,

$$\frac{\partial}{\partial t}\hat{\rho}(t) = -\frac{\mathrm{i}}{\hbar}[\hat{H},\hat{\rho}], \tag{50}$$

where $\hat{\rho}$ and $\hat{H}$ are the density matrix and the Hamiltonian of the composite system. Applying the definition (49), we obtain [11]

$$\frac{\partial}{\partial t}\hat{\rho}^{\mathrm{W}}(Q,P,t) = -\frac{\mathrm{i}}{\hbar}\Big(\hat{H}^{\mathrm{W}}\mathrm{e}^{\hbar\overleftrightarrow{\Lambda}/2\mathrm{i}}\hat{\rho}^{\mathrm{W}} - \hat{\rho}^{\mathrm{W}}\mathrm{e}^{\hbar\overleftrightarrow{\Lambda}/2\mathrm{i}}\hat{H}^{\mathrm{W}}\Big), \tag{51}$$

where we defined an operator $\overleftrightarrow{\Lambda}$ that may be written in terms of the Poisson brackets $\{\bullet,\bullet\}$:

$$\hat{A}^{\mathrm{W}}\overleftrightarrow{\Lambda}\hat{B}^{\mathrm{W}} = \frac{\partial\hat{A}^{\mathrm{W}}}{\partial P}\frac{\partial\hat{B}^{\mathrm{W}}}{\partial Q} - \frac{\partial\hat{A}^{\mathrm{W}}}{\partial Q}\frac{\partial\hat{B}^{\mathrm{W}}}{\partial P} = -\{\hat{A}^{\mathrm{W}},\hat{B}^{\mathrm{W}}\}. \tag{52}$$

Even though it is exact, Eq. (51) can only be used in practice once the exponential operators are expanded. Expanding them to the second order in $\hbar$, one obtains the *Quantum–classical Liouville Equation (QCLE)* [11, 44]:

$$\frac{\partial}{\partial t}\hat{\rho}^{\mathrm{W}}(Q,P,t) = -\frac{\mathrm{i}}{\hbar}[\hat{H}^{\mathrm{W}},\hat{\rho}^{\mathrm{W}}] + \frac{1}{2}\Big(\{\hat{H}^{\mathrm{W}},\hat{\rho}^{\mathrm{W}}\} - \{\hat{\rho}^{\mathrm{W}},\hat{H}^{\mathrm{W}}\}\Big) + \mathcal{O}(\hbar^2). \tag{53}$$

Here, the symbols Q and P stand for the sets of all bath coordinates and momenta that result by taking a multidimensional analogue of the transformation (49). It is interesting to note that in the classical limit, the operators become functions and the QCLE becomes exactly the classical Liouville equation [45]. Another important observation is that the QCLE is exact (i.e., correct not only to $\mathcal{O}(\hbar^2)$) for harmonic baths such as the one defined in Eq. (12) and if the system–bath coupling is linear as in Eq. (13).

Solving the QCLE exactly, however, does not seem feasible because Eq. (53) is really a system of partial differential equations containing as many classical variables as there are bath DOFs. What one may achieve by working with the QCLE rather than the fully quantum Liouville–von Neumann equation is a more favourable scaling of the solution as the subsystem and bath sizes increase. In the next section, we will therefore introduce an approximate solution of the QCLE.

1.4.2 Forward-backward trajectory solution

As mentioned in the beginning of this section, a method that relies on the MC integration is desirable if one wishes to simulate Stark fluorescence spectra that require calculating the orientational average. A quantum–classical method that meets this criterion is the *Forward-backward Trajectory Solution (FBTS)* proposed by Hsieh and Kapral [46]. We will briefly outline the idea behind this method below.

Any operator $\hat{A}$ in the Heisenberg picture satisfies the same form of equation as the Liouville–von Neumann equation (50), except for the opposite sign. We can thus write the QCLE (53) for a partially Wigner-transformed operator $\hat{A}^{\mathrm{W}}$ as

$$\frac{\partial}{\partial t}\hat{A}^{\mathrm{W}}(Q,P,t) = \frac{\mathrm{i}}{\hbar}\left(\overrightarrow{\mathcal{H}}\hat{A}^{\mathrm{W}} - \hat{A}^{\mathrm{W}}\overleftarrow{\mathcal{H}}\right), \tag{54}$$

where we introduce the 'forward' and 'backward' operators

$$\overrightarrow{\mathcal{H}} = \hat{H}^{\mathrm{W}}\left(1 + \frac{\hbar\overleftrightarrow{\Lambda}}{2\mathrm{i}}\right), \quad \overleftarrow{\mathcal{H}} = \left(1 + \frac{\hbar\overleftrightarrow{\Lambda}}{2\mathrm{i}}\right)\hat{H}^{\mathrm{W}}. \tag{55}$$

The formal solution of this equation follows as

$$\hat{A}^{\mathrm{W}}(Q,P,t) = \hat{\mathcal{S}}\left(\mathrm{e}^{\mathrm{i}\overrightarrow{\mathcal{H}}t/\hbar}\hat{A}^{\mathrm{W}}(Q,P,0)\mathrm{e}^{-\mathrm{i}\overleftarrow{\mathcal{H}}t/\hbar}\right), \tag{56}$$

where $\hat{A}^{\mathrm{W}}(Q,P,0)$ is the initial Wigner-transformed operator, and the ordering operator $\hat{\mathcal{S}}$ ensures the proper order in which the forward and backward operators act.

The next key step it to switch to the *Stock–Thoss mapping basis* [47–49] which allows one to describe the quantum subsystem consisting of N_{el} states $|n\rangle$ in terms of N_{el} fictitious harmonic oscillators. Using the occupation number notation, the mapping may be expressed as

$$|n\rangle \to |n\rangle_{\mathrm{M}} \equiv |0_1 \ldots 1_n \ldots 0_{N_{\mathrm{el}}}\rangle_{\mathrm{M}}\,. \tag{57}$$

In the Hilbert space of these oscillators, we have the usual creation and annihilation operators which may be written in terms of the coordinate ($\hat{q}_n$) and momentum ($\hat{p}_n$) operators of the same Hilbert space as

$$\hat{a}_n^\dagger = \frac{1}{\sqrt{2}}(\hat{q}_n - \mathrm{i}\hat{p}_n), \quad \hat{a}_n = \frac{1}{\sqrt{2}}(\hat{q}_n + \mathrm{i}\hat{p}_n), \tag{58}$$

whose action is defined as $\hat{a}_n^\dagger|0\rangle_{\mathrm{M}} = |n\rangle_{\mathrm{M}}$, $\hat{a}_n|n\rangle_{\mathrm{M}} = |0\rangle_{\mathrm{M}}$. An arbitrary operator of the mapping basis can now be expressed in terms of the elements of the same operator in the subsystem space:

$$\hat{A}_{\mathrm{M}} = \sum_{n,n'} A_{nn'}\hat{a}_n^\dagger\hat{a}_{n'}. \tag{59}$$

Finally, we introduce the coherent states of the mapping basis defined as

$$\hat{a}_n|z\rangle = z_n|z\rangle\,, \quad z_n = \frac{1}{\sqrt{2}}(q_n + \mathrm{i}p_n), \tag{60}$$

which may be used to obtain the mean values of coordinates and momenta of the oscillators:

$$q_n(t) = \langle z|\, \hat{q}_n \,|z\rangle\,, \quad p_n(t) = \langle z|\, \hat{p}_n \,|z\rangle\,. \tag{61}$$

To proceed with the derivation, we split the propagators in Eq. (56) into K short-time propagators,

$$\hat{A}^{\mathrm{W}}(Q,P,t) = \hat{\mathcal{S}}\Big(\mathrm{e}^{-\mathrm{i}\Delta t_1 \overrightarrow{\mathcal{H}}/\hbar} \ldots \hat{\mathcal{S}}\Big(\mathrm{e}^{-\mathrm{i}\Delta t_K \overrightarrow{\mathcal{H}}/\hbar} \hat{A}^{\mathrm{W}}(Q,P,0) \mathrm{e}^{\mathrm{i}\Delta t_K \overleftarrow{\mathcal{H}}/\hbar}\Big) \ldots \mathrm{e}^{\mathrm{i}\Delta t_1 \overleftarrow{\mathcal{H}}/\hbar}\Big). \tag{62}$$

and insert the resolution of identity for coherent states,

$$\hat{I} = \int \frac{\mathrm{d}^2 z}{\pi^{N_{\mathrm{el}}}} \,|z\rangle\langle z|\,, \tag{63}$$

between the exponential propagators. The resulting multi-dimensional integration, however, cannot be performed analytically because the coherent states form an over-complete basis, with the inner product of such states being

$$\langle z|z'\rangle = \exp\Big(-\frac{1}{2}|z-z'|^2 - \mathrm{i}\Im(z\cdot z'^*)\Big). \tag{64}$$

Nevertheless, we may invoke the orthogonality approximation on the coherent states by letting

$$\langle z_j(t_j)|z_{j+1}\rangle \approx \pi^{N_{\mathrm{el}}} \delta\Big(z_{j+1} - z_j(t_j)\Big), \tag{65}$$

where $\delta(z)$ is the Dirac delta-function. As we can see from Eq. (64), this approximation is reasonable if the phase space coordinates of the coherent states differ significantly. Thus the intermediate integration is greatly simplified, yielding the following formula for the evolution of the matrix elements of $\hat{A}^{\mathrm{W}}$ [46]:

$$\begin{aligned} A^{\mathrm{W}}_{nn'}(Q,P,t) = \frac{1}{4}\sum_{m,m'} \int \mathrm{d}q\,\mathrm{d}p\,\mathrm{d}q'\mathrm{d}p' (2\pi)^{-2N_{\mathrm{el}}} \exp\Big(-\frac{1}{2}\sum_{k=1}^{N_{\mathrm{el}}}(q_k^2+p_k^2+q_k'^2+p_k'^2)\Big) \\ \times (q_n + \mathrm{i}p_n)(q'_{n'} - \mathrm{i}p'_{n'}) A^{\mathrm{W}}_{mm'}(Q_t,P_t,0)\Big(q_m(t) - \mathrm{i}p_m(t)\Big)\Big(q'_{m'}(t) + \mathrm{i}p'_{m'}(t)\Big). \end{aligned} \tag{66}$$

Here, $A^{\mathrm{W}}_{mm'}(Q_t,P_t,0)$ is the element (m,m') of the initial value of the operator $\hat{A}^{\mathrm{W}}(Q,P,0)$ where the coordinates and momenta are taken at time t. The subsystem and bath phase space coordinates are propagated using a set of Hamilton equations [46]:

$$\begin{aligned} \frac{\mathrm{d}}{\mathrm{d}t}q_m &= \frac{1}{\hbar}\frac{\partial}{\partial p_m} H_{\mathrm{cl}}(Q,P,q,p), & \frac{\mathrm{d}}{\mathrm{d}t}p_m &= -\frac{1}{\hbar}\frac{\partial}{\partial q_m} H_{\mathrm{cl}}(Q,P,q,p), \\ \frac{\mathrm{d}}{\mathrm{d}t}q'_m &= \frac{1}{\hbar}\frac{\partial}{\partial p'_m} H_{\mathrm{cl}}(Q,P,q',p'), & \frac{\mathrm{d}}{\mathrm{d}t}p'_m &= -\frac{1}{\hbar}\frac{\partial}{\partial q'_m} H_{\mathrm{cl}}(Q,P,q',p'), \\ \frac{\mathrm{d}}{\mathrm{d}t}Q_{m\mu} &= \frac{1}{\hbar}\frac{\partial}{\partial P_{m\mu}} H_{\mathrm{eff}}(Q,P,q,p,q',p'), & \frac{\mathrm{d}}{\mathrm{d}t}P_{m\mu} &= -\frac{1}{\hbar}\frac{\partial}{\partial Q_{m\mu}} H_{\mathrm{eff}}(Q,P,q,p,q',p'). \end{aligned} \tag{67}$$

Here, we defined the following 'classical' and 'combined' Hamiltonians:

$$H_{\rm cl}(Q,P,q,p) = H_{\rm B}^{\rm W} + \frac{1}{N_{\rm el}}{\rm Tr}_{\rm S}(\hat{H}_{\rm S} + \hat{H}_{\rm SB}^{\rm W}) + \frac{1}{2}\sum_{n,n'} h_{nn'}^{\rm W}(q_n q_{n'} + p_n p_{n'}), \tag{68}$$

where

$$\hat{h} = \hat{H}_{\rm S} + \hat{H}_{\rm SB} - {\rm Tr}_{\rm S}(\hat{H}_{\rm S} + \hat{H}_{\rm SB}), \tag{69}$$

and

$$H_{\rm comb}(Q,P,q,p,q',p') = \frac{1}{2}\Big(H_{\rm cl}(Q,P,q,p) + H_{\rm cl}(Q,P,q',p')\Big). \tag{70}$$

In the system of equations (67), the trajectories $q_m(t)$, $p_m(t)$, $q'_m(t)$, and $p'_m(t)$ correspond to the m-th subsystem state, while $Q_{m\mu}(t)$ and $P_{m\mu}(t)$ describe the dynamics of the μ-th bath oscillator attached to the m-th subsystem state. The total number of equations follows as $n_{\rm eqs} = 4N_{\rm el} + 2N_{\rm el}N_{\rm osc}$, which shows that the method scales linearly with the number of electronic (subsystem) states. The latter fact is an important advantage of the FBTS, which is essentially achieved through the classical description of the bath. The main disadvantage of the method, which is perhaps less obvious, lies in the physical abstractness of the orthogonality approximation (65). While this is the only approximation used to arrive at the final solution, its interpretation is rather ambiguous. Consequently, it is not possible to establish the region of validity of the method (depending on the system parameters) analytically, and some testing is required. This issue has been studied in Ref. [50], where the FBTS has been applied for the calculation of system dynamics and general trends have been determined. However, a separate analysis is needed to assess the accuracy of calculations of spectra.

Once we have found the evolution of the required operator, we may calculate the expectation value of the corresponding observable as

$$A(t) = {\rm Tr}\Big(\hat{A}(t)\hat{\rho}\Big) = \int {\rm d}Q\,{\rm d}P\,{\rm Tr}_{\rm S}\Big(\hat{A}^{\rm W}(Q,P,t)\hat{\rho}^{\rm W}(Q,P)\Big), \tag{71}$$

where $\hat{\rho}^{\rm W}(X)$ is the partially Wigner-transformed initial density matrix of the composite system. The integration over the classical variables Q and P essentially corresponds to tracing over the bath DOFs. If we substitute the expression for $\hat{A}^{\rm W}(Q,P,t)$ from Eq. (66), we obtain an integral whose dimensionality is $n_{\rm eqs}$. Even for a typical small problem, we have $N_{\rm el} = 2$ and $N_{\rm osc} = 50$, resulting in $n_{\rm eqs} = 204$. Therefore, one has to resort to the MC integration, generating the phase space variables randomly, calculating the integrand, and averaging the results. Notably, the convergence is enhanced by the exponential factor in Eq. (66) which ensures that only a small part of the subsystem phase space is relevant for the calculation. As we show below, the initial bath density matrix in Eq. (71) also has an exponential form, so that overall convergence is satisfactory. Furthermore, high dimensionality of the problem may be turned to our advantage when additional orientational averaging is required: adding three more integration dimensions will have no noticeable impact on the calculation time when the original problem already has more than 100 dimensions.

1.4.3 Application to spectroscopic calculations

According to Eq. (71), the dipole–dipole correlation function (31) may be calculated as

$$C_{\mathrm{d-d}}(t) = \int \mathrm{d}Q\,\mathrm{d}P\,\mathrm{Tr}_{\mathrm{S}}\Big(\Big(\hat{\boldsymbol{\mu}}^{\mathrm{I}}(t;Q,P)\cdot\boldsymbol{\sigma}_E\Big)\Big(\hat{\boldsymbol{\mu}}^{\mathrm{I}}(0)\cdot\boldsymbol{\sigma}_E\Big)\hat{\rho}^{\mathrm{W}}_{\mathrm{SB}}(Q,P,0)\Big). \tag{72}$$

Here, the dipole moment operator $\hat{\boldsymbol{\mu}}^{\mathrm{I}}(0)$ is a subsystem operator, and initially, its partial Wigner transform with respect to the bath is identically equal to itself. The evolution of the dipole moment may be calculated using the FBTS formula (67), which makes the operator depend on the bath coordinates and momenta parametrically. One sees this by considering the fact that $\hat{\boldsymbol{\mu}}^{\mathrm{I}}(t;Q,P)$ is given by a combination of subsystem variables $q_m(t)$, $p_m(t)$, $q'_m(t)$, and $p'_m(t)$ which are obtained by solving the equations (67) where the initial conditions for the bath variables Q and P have to be specified.

The first step of calculation of the spectrum is to find the partial Wigner transform of the excited state equilibrium density matrix $\hat{\rho}^{\mathrm{W}}_{\mathrm{SB}}(Q,P,0)$ using the FBTS formula. At the initial time moment $t = t_0$, right after the system is excited, it is reasonable to assume that the subsystem and the bath are uncorrelated, meaning that the initial density matrix may be factorised into subsystem and bath parts,

$$\hat{\rho}_{\mathrm{SB}}(t_0) = \hat{\rho}_{\mathrm{S}}(t_0)\hat{\rho}_{\mathrm{B}}(t_0), \tag{73}$$

with the same factorisation holding for $\hat{\rho}^{\mathrm{W}}_{\mathrm{SB}}(Q,P,t_0)$. The system is taken to occupy the ground state $|0\rangle$ at $t = t_0$, while the bath oscillators are taken to be in thermal equilibrium, so that the canonical energy distribution may be assumed, resulting in

$$\hat{\rho}_{\mathrm{B}}(t_0) = \prod_{n=1}^{N_{\mathrm{el}}}\prod_{\nu=1}^{N_{\mathrm{osc}}}\frac{1}{\mathcal{Z}_{n\nu}}\exp\left(-\frac{\beta\hbar\omega_{n\nu}}{2}(\hat{X}^2_{n\nu}+\hat{P}^2_{n\nu})\right), \tag{74}$$

where $\mathcal{Z}_{n\nu}$ is the partition function for the oscillator with frequency $\omega_{n\nu}$. Carrying out the Wigner transformation, one obtains [27]

$$\rho^{\mathrm{W}}_{\mathrm{B}}(Q,P,t_0) = \prod_{n=1}^{N_{\mathrm{el}}}\prod_{\nu=1}^{N_{\mathrm{osc}}}\frac{1}{\pi}\tanh\left(\frac{\beta\hbar\omega_{n\nu}}{2}\right)\exp\left[-\tanh\left(\frac{\beta\hbar\omega_{n\nu}}{2}\right)(Q^2_{n\nu}+P^2_{n\nu})\right]. \tag{75}$$

Finally, we have to write down the Hamilton equations (67) for the chosen Hamiltonians (4), (13), and (12). The partial Wigner transformations of the latter two operators follow trivially using $\hat{X}^{\mathrm{W}} = Q$ and $\hat{P}^{\mathrm{W}} = P$, and the partial differentiations yield

$$\frac{\mathrm{d}}{\mathrm{d}\tau}q_m = \frac{p_m}{\gamma}\mathcal{A}_m + \frac{1}{\hbar\gamma}\sum_{n\neq m} J_{mn}p_n, \quad \frac{\mathrm{d}}{\mathrm{d}\tau}p_m = -\frac{q_m}{\gamma}\mathcal{A}_m - \frac{1}{\hbar\gamma}\sum_{n\neq m} J_{mn}q_n,$$
$$\frac{\mathrm{d}}{\mathrm{d}\tau}q'_m = \frac{p'_m}{\gamma}\mathcal{A}_m + \frac{1}{\hbar\gamma}\sum_{n\neq m} J_{mn}p'_n, \quad \frac{\mathrm{d}}{\mathrm{d}\tau}p'_m = -\frac{q'_m}{\gamma}\mathcal{A}_m - \frac{1}{\hbar\gamma}\sum_{n\neq m} J_{mn}q'_n,$$
$$\frac{\mathrm{d}}{\mathrm{d}\tau}Q_{m\mu} = \frac{\omega_{m\mu}}{\gamma}P_{m\mu}, \tag{76}$$
$$\frac{\mathrm{d}}{\mathrm{d}\tau}P_{m\mu} = -\frac{\omega_{m\mu}}{\gamma}\left[Q_{m\mu} - \frac{d_{m\mu}}{4}\left(q_m^2 + p_m^2 + q_m'^2 + p_m'^2 + \frac{4}{N_\mathrm{el}}\right) + \frac{d_{m\mu}}{4N_\mathrm{el}}\sum_{n=0}^{N_\mathrm{el}}(q_n^2 + p_n^2 + q_n'^2 + p_n'^2)\right].$$

Here, we use the dimensionless time $\tau = t\gamma$ measured in units of the spectral density parameter γ (see Eq. (19)), and we define

$$\mathcal{A}_m = \frac{\varepsilon'_m}{\hbar} - \sum_{\nu=1}^{N_\mathrm{osc}}(1-\delta_{0,m})\omega_{m\nu}d_{m\nu}Q_{m\nu} - \frac{1}{N_\mathrm{el}\hbar}\sum_{n=0}^{N_\mathrm{el}}\left(\varepsilon'_m - \sum_{\nu=1}^{N_\mathrm{osc}}(1-\delta_{0,n})\hbar\omega_{n\nu}d_{n\nu}Q_{n\nu}\right). \tag{77}$$

The variables ε'_m are the energies of the subsystem states, which are shifted if an external electric field is present:

$$\varepsilon'_m = \varepsilon_m - \Delta\boldsymbol{\mu}_{mm}\cdot\boldsymbol{\mathcal{E}}. \tag{78}$$

Unfortunately, direct application of the FBTS formula (66) with $\hat{A} = \hat{\rho}_\mathrm{SB}$ turns out to be inefficient, as the contribution of the majority of MC trajectories becomes very small because of the term $\rho^\mathrm{W}_{\mathrm{SB}mm'}(Q_t, P_t, 0)$. Indeed, as the system evolves, the phase space coordinates Q and P begin oscillating with considerable amplitudes, which results in small values of the said term given its Gaussian-like dependence on Q and P (see Eq. (75)). Converged results of the density matrix of the composite system can only be obtained if the subsystem–bath interaction is rather weak [51], which is definitely not the regime of actual interest. To circumvent this issue, we may invoke an approximation and assume that the separation (73) holds not only at $t = t_0$ but also at $t = 0$. Then, Eq. (72) becomes

$$C_\mathrm{d-d}(t) = \int \mathrm{d}Q\,\mathrm{d}P\,\rho^\mathrm{W}_\mathrm{B}(Q,P,0)\mathrm{Tr}_\mathrm{S}\Big(\big(\hat{\boldsymbol{\mu}}^\mathrm{I}(t;Q,P)\cdot\boldsymbol{\sigma}_E\big)\big(\hat{\boldsymbol{\mu}}^\mathrm{I}(0)\cdot\boldsymbol{\sigma}_E\big)\hat{\rho}_\mathrm{S}(0)\Big). \tag{79}$$

Here, the bath density matrix $\rho^\mathrm{W}_\mathrm{B}(Q,P,0)$ is just the time-dependent distribution function of the bath trajectories $Q(t)$ and $P(t)$, which are found by propagating the Hamilton equations. The subsystem density matrix $\hat{\rho}_\mathrm{S}(0)$ is still not known at this point, but, contrary to the composite density operator $\hat{\rho}_\mathrm{SB}$, it may be calculated efficiently using the FBTS formula.

Thus, the algorithm for calculating the Stark fluorescence spectrum is the following. First, we generate a set of variables q, p, q', p', Q, P and the three Euler angles for the orientational averaging, and propagate the system density matrix until equilibrium is reached to obtain $\hat{\rho}_\mathrm{S}(0)$. Since the bath oscillators are propagated simultaneously with the subsystem variables, the bath density matrix $\rho^\mathrm{W}_\mathrm{B}(Q,P,0)$ is obtained in the process as well. Next, we propagate the dipole moment operator for a set period of time that ensures that the correlation function will

have decayed considerably by the end of this period. This procedure (finding the equilibrium and propagating the dipole moment) has to be repeated twice — once with an external field, and then without it. According to the MC integration method, all of the described operations have to be repeated numerous times with different initial conditions, and the results should be averaged. Having obtained the averaged dipole–dipole correlation function, it only remains to perform its Fourier transform as given by Eq. (36).

To perform the calculations, we wrote a parallel computer program that is adapted for running on high performance computers. The source code is available on Gitlab[9].

[9] https://gitlab.com/jakovbraver/fbts

2 Simulations

In this section, we will present and analyse the modelled Stark fluorescence spectra with several goals in mind. First, we wish to evaluate whether the FBTS allows one to obtain sufficiently accurate or at least qualitatively correct results. Second, it is interesting to test the Liptay formalism (43) — while it is actively used for analysing the Stark spectra, there are no published works that compare this model with the exact results. Finally, we will study how the presence of a CT state in the system influences the Stark fluorescence spectra.

To obtain formally exact results, we used the aforementioned HEOM approach [36, 52], which by now has become one of the standard tools used for benchmarking other methods. The HEOM, however, has several serious drawbacks. First, it produces exact results only for a limited set of spectral densities (the Debye spectral density (19) being one of them), and therefore cannot be used for simulating arbitrary realistic systems. Second, the method scales unfavourably as the subsystem size increases, making it impractical for subsystems with more than ten electronic levels. The scalability of HEOM becomes even more of a problem when calculating the Stark fluorescence spectra as the orientational averaging further increases the calculation time.

The spectra calculated using HEOM, FBTS, and the Liptay formula (43) were normalised as follows. The field-free HEOM fluorescence spectra were normalised so that the maximum of intensity coincides with the FBTS result. The same scaling factor was then used to rescale the Stark fluorescence spectra obtained using HEOM. The Liptay formula was used by differentiating the HEOM fluorescence spectra (which are considered exact), and each resulting curve was rescaled so that its minimum value matches the HEOM result. In cases when the Liptay formula yielded curves whose shapes are drastically different from the HEOM results, the Liptay spectra were simply normalised in a way that makes them visible at the chosen scale.

To gain more insight into the calculated spectra, especially when a CT state is present in the system, it will prove useful to calculate the equilibrium values of subsystem state energies and populations. The energies may be found approximately as the eigenenergies of the subsystem Hamiltonian $\hat{H}_{\mathrm{S}}$; the populations are then given by the diagonal elements of the system density matrix $\hat{\rho}_{\mathrm{S}} = \mathrm{e}^{-\beta\hat{H}_{\mathrm{S}}}/\mathrm{Tr}(\mathrm{e}^{-\beta\hat{H}_{\mathrm{S}}})$, where $\hat{H}_{\mathrm{S}}$ is assumed to be diagonalised. Such a calculation, however, totally neglects the presence of the bath and may be inadequate if the system–bath coupling is strong. A more accurate approximation for the equilibrium state of the subsystem has been derived in Ref. [53]. There, it is shown that the equilibrium subsystem density operator is given by the familiar Boltzmann distribution,

$$\hat{\rho}_{\mathrm{S}} \approx \frac{\mathrm{e}^{-\beta\hat{H}_{\mathrm{eff}}}}{\mathrm{Tr}(\mathrm{e}^{-\beta\hat{H}_{\mathrm{eff}}})}, \tag{80}$$

calculated using the following effective Hamiltonian:

$$\hat{H}_{\mathrm{eff}} = \hat{H}_{\varepsilon} - \hat{\Lambda} + \mathrm{e}^{-\beta\hat{\Lambda}/6}\hat{H}_{J}\mathrm{e}^{-\beta\hat{\Lambda}/6}, \tag{81}$$

where $\hat{H}_\varepsilon$ and $\hat{H}_J$ are, respectively, the diagonal and off-diagonal parts of $\hat{H}_\mathrm{S}$, and $\hat{\Lambda} = \mathrm{diag}(\{\lambda_n\})$. As we can see, the influence of the bath comes down to a change of the resonance couplings between subsystem states. Correspondingly, the energies of the subsystem states are given by the eigenvalues of $\hat{H}_\mathrm{eff}$. Even though the formula (81) presents an approximation that breaks down in the limits of low temperatures or very strong system–bath interaction strengths [53], it can be considered correct for all the cases that we will study. Following Ref. [53], we will refer to the basis in which $\hat{H}_\mathrm{eff}$ is diagonal as the *global basis*.

2.1 Systems with two molecular-excitation states

We begin the analysis by studying the spectra of a family of systems with similar parameters for the purpose of testing the FBTS method. The parameters have been chosen to resemble those typical for the photosynthetic complexes [16]:

$$\Delta\varepsilon \equiv \varepsilon_2 - \varepsilon_1 = 100\,\mathrm{cm}^{-1}, \quad J = 100\,\mathrm{cm}^{-1}, \quad \lambda = 50\,\mathrm{cm}^{-1}, \quad \gamma^{-1} = 100\,\mathrm{fs}, \quad T = 300\,\mathrm{K}. \tag{82}$$

In this model, we have a ground state $|0\rangle$ and two excited states, $|1\rangle$ and $|2\rangle$, both of which are molecular excitations. The energy gap between the ground state and the lowest excited state is $\varepsilon_1 - \varepsilon_0 = 15000\,\mathrm{cm}^{-1}$, while the energy difference $\Delta\varepsilon$ between the excited states is given above. The resonance coupling between the states is denoted by $J \equiv J_{12}$. Throughout the analysis, we will often specify the parameters of the subsystem by providing the subsystem Hamiltonian; for the present case it would take the form

$$\hat{H}_\mathrm{S} = \begin{pmatrix} \varepsilon_1 & J_{12} \\ J_{12} & \varepsilon_2 \end{pmatrix} = \begin{pmatrix} 0 & 100 \\ 100 & 100 \end{pmatrix}. \tag{83}$$

In this notation, the ground state is ignored for brevity (it would correspond to an additional row and an additional column), and the energy gap $\varepsilon_1 - \varepsilon_0$ is subtracted from the site energies (e.g., the energy of state $|2\rangle$ is actually $15100\,\mathrm{cm}^{-1}$). For clarity, we note that site-basis states $|1\rangle$ and $|2\rangle$ correspond to the states of uncoupled monomers; they are the eigenstates of Hamiltonian (83) taken with $J_{12} = 0$.

The chosen value of the system–bath coupling strength λ corresponds to the intermediate coupling regime, and the coupling is the same for both states: $\lambda_1 = \lambda_2 = \lambda$. The relaxation constant γ^{-1} is taken to be large enough so that the dynamics may be considered non-Markovian and therefore arguably less trivial.

The strength of the external electric field is chosen to be $|\boldsymbol{\mathcal{E}}| = 3\,\mathrm{MV/cm}$ so that the Stark effect is pronounced. This is in line with the strengths of the field used in the actual experiments, where the value varies from 0.3 to $2\,\mathrm{MV/cm}$ [2, 7, 9]. Choosing a greater value is also more convenient when numerous calculations have to be performed because it speeds up convergence of both HEOM and FBTS. Values that are closer to those used in the experiments would require up to an order of magnitude more calculation time, but that is acceptable when only a couple of simulations (of a real experiment) have to be performed. The transition dipole

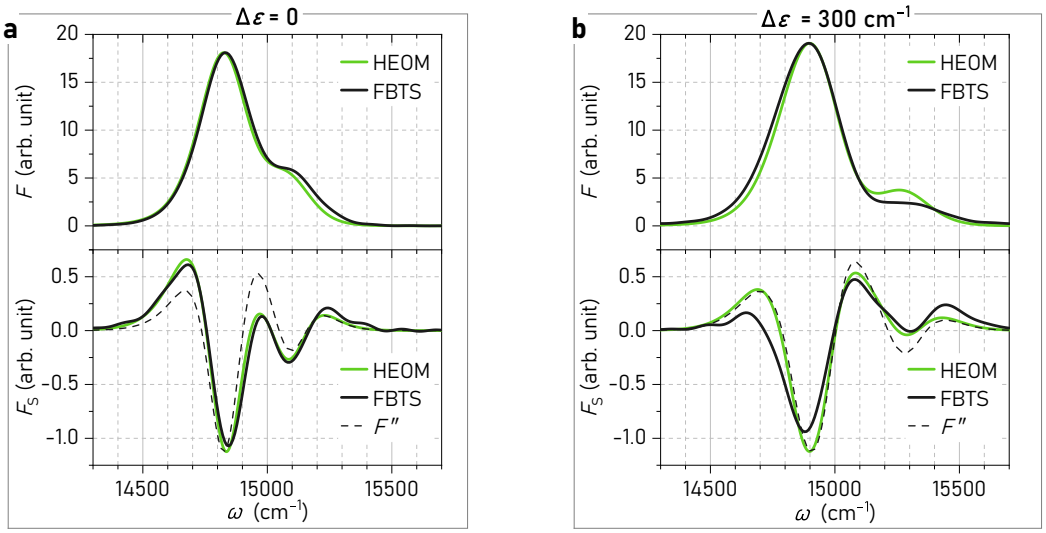

Figure 2: Fluorescence spectra (top) and Stark fluorescence spectra (bottom) calculated using HEOM and FBTS. The dashed lines represent the second derivatives of the corresponding fluorescence spectra. Two cases are shown: **(a)** $\Delta\varepsilon = 0$, **(b)** $\Delta\varepsilon = 300\,\mathrm{cm}^{-1}$.

moments used in the simulations are $\boldsymbol{\mu}_{01} = (1, 0, 0)$ and $\boldsymbol{\mu}_{02} = (0, 1, 0)$, and the static dipole moments are $\Delta\boldsymbol{\mu}_{11} = (1.5, 0, 0)$ and $\Delta\boldsymbol{\mu}_{22} = (0, 1.5, 0)$; the values are given in the Debye units.

We will test the FBTS by varying one of the parameters while others will be set equal to their 'default' values (82). We start with the analysis of two edge cases for the energy gap $\Delta\varepsilon$ shown in Fig. 2. The upper graphs contain the fluorescence spectra, and the lower plots show the Stark fluorescence spectra. The intensities are given in arbitrary units, with the same ones used for all the graphs allowing for an evaluation of the magnitude of the Stark effect. In the upper part of Fig. 2a, corresponding to the case of degenerate levels, $\Delta\varepsilon = 0$, we can see that the FBTS captures the positions of the peaks and their relative intensities accurately. While not completely resolved, two rather than one spectral bands are obtained because the interaction between monomers (J) removes the degeneracy of the levels. The theoretical values of the peak positions may be found using the effective coupling formalism, Eq. (81). The eigenvalues of $\hat{H}_{\mathrm{eff}}$ for the system under consideration (neglecting the bias of $15000\,\mathrm{cm}^{-1}$) are $-42\,\mathrm{cm}^{-1}$ and $142\,\mathrm{cm}^{-1}$ which is close to the exact results predicted by HEOM. In the lower part of Fig. 2a, we notice that the FBTS yields the Stark fluorescence spectrum with a similar accuracy. The positions of the two minima coincide with the positions of the maxima seen in the corresponding fluorescence spectrum, which is in line with the HEOM results. According to the definition (38), the negative parts of F_{S} indicate the reduction of intensity when an external field is introduced, while the positive parts signify an increase of intensity. In the present case, the effect is rather weak — the intensity of the maximum of the stronger fluorescence band decreases by approximately 6% in an external field. Looking at the dashed line that shows the second derivative of F, we see that its shape has some noticeable disagreements with the results obtained using the two other methods. This could result in the static dipole moments of the system being determined incorrectly using Eq. (44). A different situation is seen when the energy gap between levels is large, $\Delta\varepsilon = 300\,\mathrm{cm}^{-1}$, which is shown in Fig. 2b. In the lower

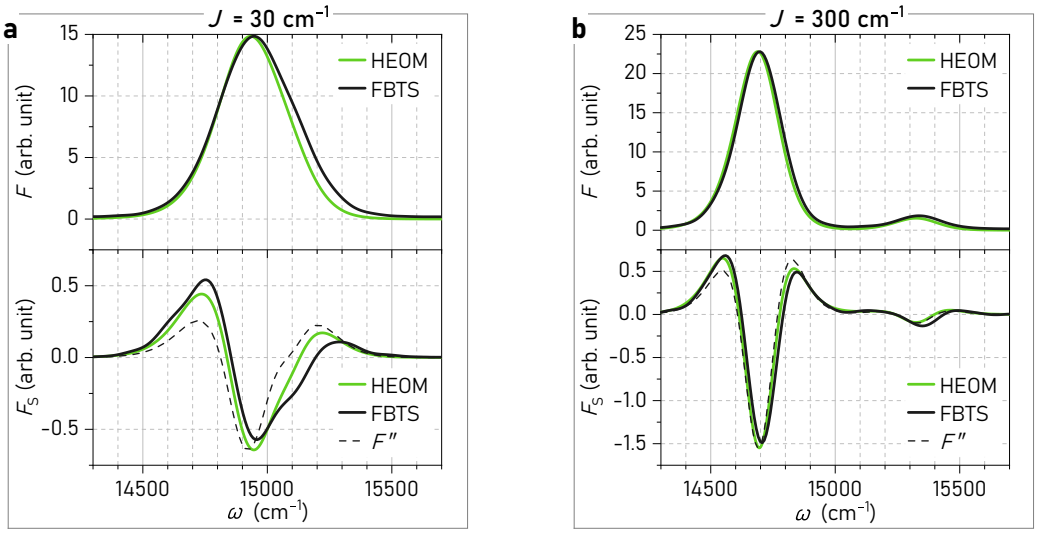

Figure 3: Same as Fig. 2 for the cases **(a)** $J = 30\,\mathrm{cm}^{-1}$, **(b)** $J = 300\,\mathrm{cm}^{-1}$.

part, we can see that this time the agreement between the exact HEOM results and the F'' curve is noticeably better, while the FBTS results are less accurate. This can be traced down to the fact that the corresponding fluorescence spectrum is also calculated less accurately than in the case of degenerate levels. Therefore, we conclude that the error in the FBTS calculations increases as the energy gap increases. For molecules with a certain orientation, the external electric field causes an even higher separation of the levels, which further reduces the accuracy of FBTS leading to a less accurate Stark fluorescence spectrum.

Now let us consider the variation of the resonance coupling strength J. The analysis of the case $J = 30\,\mathrm{cm}^{-1}$ is shown in Fig. 3a. In the fluorescence spectrum, we notice that the weak coupling does not separate the energy levels enough for two peaks to be visible. Indeed, the eigenenergies predicted by the effective coupling theory (81) are $\pm 57\,\mathrm{cm}^{-1}$, and the spectral bands are too broad for the peaks to be resolvable. Speaking of the accuracy of FBTS, the method provides the results that are close the exact ones. The Stark fluorescence spectrum, on the other hand, is calculated less accurately, but qualitative correctness is certainly achieved. Turning to the regime of strong molecular coupling, $J = 300\,\mathrm{cm}^{-1}$, the FBTS performs better at calculating both types of spectra as demonstrated in Fig. 3b. The second derivative also provides a better fit of the Stark fluorescence spectrum, which can be attributed to the fact that the bands corresponding to the different transitions are well-separated.

Finally, the dependence of the accuracy of FBTS on the subsystem–bath interaction strength has to be investigated. In Fig. 4a we can see that the quantum-classical method works very well when the subsystem interacts weakly ($\lambda = 10\,\mathrm{cm}^{-1}$) with the bath, although the fluorescence intensity of the high-frequency band is underestimated, leading to similar discrepancies in the Stark fluorescence spectrum. The Liptay formalism is also certainly applicable in this regime as the exact HEOM results indeed follow the shape of F''. We also notice that the Stark effect is especially pronounced in this case — the intensity of the low-frequency band falls by almost a third when an external field is switched on. This is to be expected because for small values of λ, the bath-induced broadening of the spectral bands is small, hence the broadening due to the

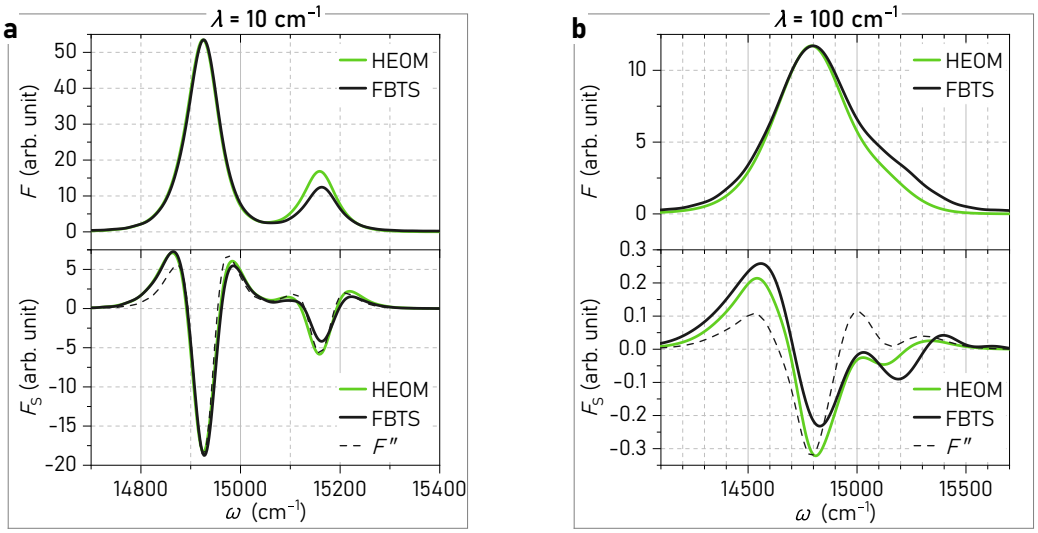

Figure 4: Same as Fig. 2 for the cases **(a)** $\lambda = 10\,\mathrm{cm}^{-1}$, **(b)** $\lambda = 100\,\mathrm{cm}^{-1}$.

external field is more noticeable. Meanwhile, strong interaction with the bath leads to relatively weak intensity of the Stark fluorescence spectrum as shown in Fig. 4b, corresponding to the case $\lambda = 100\,\mathrm{cm}^{-1}$. This case poses difficulties for the FBTS as the shape of the calculated Stark fluorescence spectrum differs appreciably from the HEOM results. This is especially true in the region of the higher frequencies, where the fluorescence spectrum is also calculated inaccurately. The second derivative curve likewise does not provide a reasonable fit of the exact results.

In summary, the results of this section show that the FBTS is generally applicable for calculating the Stark fluorescence spectra. The dependence of the accuracy on the system parameters is largely in line with the results of the thorough analysis performed in Ref. [50], where the FBTS was applied for the calculations of system dynamics. Specifically, we conclude that the accuracy in calculations of the Stark fluorescence spectra falls down for higher values of the energy gap ($\Delta\varepsilon$) and reorganisation energies (λ). Conversely, stronger interaction between the monomers (J) decreases the error.

2.2 Systems with one molecular-excitation state and one CT state

Now let us analyse a different model, where state $|2\rangle$ is a CT state. Such a state is described by a zero transition moment, large static dipole moment, and a strong interaction with the bath [11]. Correspondingly, we set $\boldsymbol{\mu}_{02} = (0, 0, 0)$ and $\Delta\boldsymbol{\mu}_{22} = (0, 15, 0)$, whereas λ_2 will be varied. The dipole moments of the molecular-excitation state, $|1\rangle$, are the same as in the previous section: $\boldsymbol{\mu}_{01} = (1, 0, 0)$, $\Delta\boldsymbol{\mu}_{11} = (1.5, 0, 0)$. The reorganisation energy of the first state is chosen to be rather small, $\lambda_1 = 10\,\mathrm{cm}^{-1}$, for a better contrast with the CT state. In the two following sections, we will investigate two cases where the energy of the CT state will be either lower or higher than that of the other state, which is optically bright.

A remark about notation has to be made. The global-basis eigenstates of $\hat{H}_{\mathrm{eff}}$ will be denoted as $|n\rangle_{\mathrm{GB}}$, where $n = 1, 2$. Correspondingly, the element $(0, n)$ of the dipole moment matrix $\hat{\boldsymbol{\mu}}$ transformed to the global basis will be denoted as $\boldsymbol{\mu}_{0n}^{\mathrm{GB}}$, and it will represent the transition

dipole moment from state $|n\rangle_{\mathrm{GB}}$ to the ground state $|0\rangle$, with the latter being unaffected by the transformation. Further, we note that it is a matter of choice which of the eigenstates to call $|1\rangle_{\mathrm{GB}}$ and which to call $|2\rangle_{\mathrm{GB}}$; it is only important to keep track of which state corresponds to which energy and transition dipole moment. We will adopt the convention that the state with the lower transition dipole moment in the global basis is called $|2\rangle_{\mathrm{GB}}$: $|\boldsymbol{\mu}_{02}^{\mathrm{GB}}| < |\boldsymbol{\mu}_{01}^{\mathrm{GB}}|$.

2.2.1 Case 1: $\varepsilon_{\mathrm{CT}} < \varepsilon_{\mathrm{bright}}$

We begin with the case where we set the bright state $|1\rangle$ to have higher energy than the CT state $|2\rangle$:

$$\hat{H}_{\mathrm{S}} = \begin{pmatrix} 100 & 100 \\ 100 & 0 \end{pmatrix}. \tag{84}$$

The spectra calculated using this Hamiltonian with different values of λ_2 are shown in Fig. 5. First, we consider a system where state $|2\rangle$ is not exactly a CT state because of the weak coupling with the bath, $\lambda_2 = 10\,\mathrm{cm}^{-1}$. In the fluorescence spectrum in Fig. 5a we can clearly see two separate bands, including the $\sim 14900\,\mathrm{cm}^{-1}$ band corresponding to the transition $|2\rangle_{\mathrm{GB}} \to |0\rangle$ even though the second state is optically dark. This is explained by the redistribution of the oscillator strength that takes place due to the resonance coupling. A simple calculation shows that in the global basis, the transition dipole moments redistribute as follows: $|\boldsymbol{\mu}_{01}^{\mathrm{GB}}|^2 = 0.73\,\mathrm{D}^2$, $|\boldsymbol{\mu}_{02}^{\mathrm{GB}}|^2 = 0.27\,\mathrm{D}^2$, hence the transition from state $|2\rangle_{\mathrm{GB}}$ becomes allowed. Although we obtain that $|\boldsymbol{\mu}_{02}^{\mathrm{GB}}|^2 < |\boldsymbol{\mu}_{01}^{\mathrm{GB}}|^2$, the intensity of the $|2\rangle_{\mathrm{GB}} \to |0\rangle$ transition band is nonetheless higher than that of the $|1\rangle_{\mathrm{GB}} \to |0\rangle$ transition band. This is in turn caused by a higher equilibrium population of state $|2\rangle_{\mathrm{GB}}$: $\rho_{22}^{\mathrm{GB}} = 0.74$, $\rho_{11}^{\mathrm{GB}} = 0.26$. The FBTS, however, underestimates the intensity of the high-frequency band, similarly to what we have seen in Fig. 4a. The same holds true in the Stark fluorescence spectrum, which is now quite different from the case analysed in Fig. 4a. In the lower part of Fig. 5a, we immediately notice that the Stark fluorescence spectrum definitely does not have the shape of F''. We will now show that this is due to the dependence of the equilibrium state populations on the orientation of the molecules.

When no external field is present, the subsystem Hamiltonian is given by Eq. (84), and the eigenenergies of the subsystem are

$$\varepsilon_1^{\mathrm{GB}} = 150\,\mathrm{cm}^{-1}, \quad \varepsilon_2^{\mathrm{GB}} = -70\,\mathrm{cm}^{-1} \tag{85}$$

(note that these are not the eigenvalues of $\hat{H}_{\mathrm{S}}$ from Eq. (84) but rather the eigenvalues of $\hat{H}_{\mathrm{eff}}$ from Eq. (81)). In the ensemble of molecules, some of them will be oriented in such a way so that the static dipole moment of state $|2\rangle$ is aligned with the external field when it is applied: $\Delta\boldsymbol{\mu}_{22} \uparrow\uparrow \boldsymbol{\mathcal{E}}$. In that case, the energy of state $|2\rangle$ changes by $-\Delta\boldsymbol{\mu}_{22} \cdot \boldsymbol{\mathcal{E}} = -756\,\mathrm{cm}^{-1}$, and the subsystem Hamiltonian becomes

$$\hat{H}_{\mathrm{S}}^{\uparrow\uparrow} = \begin{pmatrix} 100 & 100 \\ 100 & 0 - 756 \end{pmatrix}. \tag{86}$$

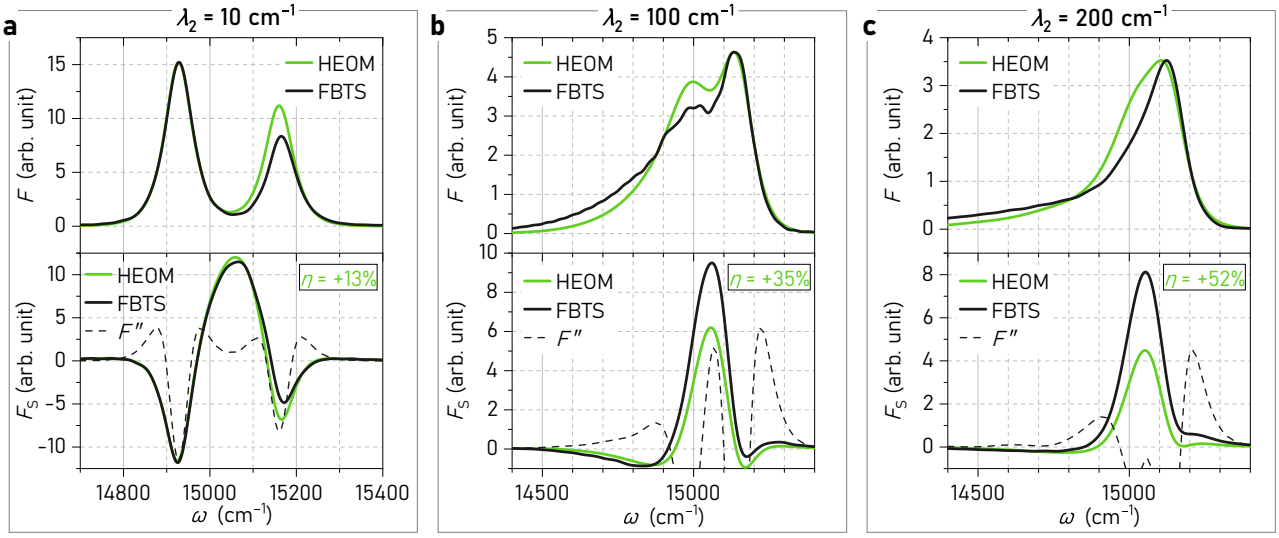

Figure 5: Spectra of systems with one bright state and one CT state, with $\varepsilon_{\mathrm{CT}} < \varepsilon_{\mathrm{bright}}$. Three cases are shown: **(a)** $\lambda_2 = 10\,\mathrm{cm}^{-1}$, **(b)** $\lambda_2 = 100\,\mathrm{cm}^{-1}$, **(c)** $\lambda_2 = 200\,\mathrm{cm}^{-1}$.

The corresponding state energies and the transition dipole moments in the global basis are

$$\begin{aligned} \varepsilon_1^{\uparrow\uparrow} &= 101\,\mathrm{cm}^{-1}, \quad \varepsilon_2^{\uparrow\uparrow} = -777\,\mathrm{cm}^{-1}, \\ |\boldsymbol{\mu}_{01}^{\uparrow\uparrow}|^2 &= 0.99\,\mathrm{D}^2, \quad |\boldsymbol{\mu}_{02}^{\uparrow\uparrow}|^2 = 0.01\,\mathrm{D}^2. \end{aligned} \tag{87}$$

It follows that in this configuration, the energy of the bright state is lower than in the absence of the field (i.e., $\varepsilon_1^{\uparrow\uparrow} < \varepsilon_1^{\mathrm{GB}}$) . Therefore, the high-frequency band shifts towards the lower frequencies. However, since $\varepsilon_1^{\uparrow\uparrow}$ is considerably higher than $\varepsilon_2^{\uparrow\uparrow}$, the population of state $|1\rangle_{\mathrm{GB}}$ is vanishingly small, so it almost does not fluoresce at all. Despite being overwhelmingly more occupied, state $|2\rangle_{\mathrm{GB}}$ barely fluoresces as well because of the small transition moment. The corresponding region of fluorescence at $\omega \sim 14223\,\mathrm{cm}^{-1}$ is not shown in Fig. 5a because the intensity is unnoticeable there at the chosen scale. Thus, if a dimer is oriented in such a way so that $\Delta\boldsymbol{\mu}_{22} \uparrow\uparrow \boldsymbol{\mathcal{E}}$, then the fluorescence intensity of the original bands (corresponding to the absence of the field) decreases, and no noticeable fluorescence appears at any other frequencies. The analysed parallel orientation corresponds to an edge case, but the results may be extended to the interval $\vartheta \in (0; \pi/2)$, where ϑ is the angle between $\Delta\boldsymbol{\mu}_{22}$ and $\boldsymbol{\mathcal{E}}$ (orientations where $\vartheta \in (\pi/2; \pi)$ will be studied below). For larger angles in this range, the difference between the state energies is not as large, resulting in appreciable population of state $|1\rangle_{\mathrm{GB}}$. Given its high transition dipole moment, that state does fluorescence, but the band shifts towards the lower frequencies. Therefore, rather than simply broadening, the fluorescence band centred at $\omega \approx 15150\,\mathrm{cm}^{-1}$ (see Fig. 5a, upper panel) undergoes a shift, causing a decrease of intensity at that frequency and an increase of intensity in the region of the lower frequencies. We note in passing that the broadening of the $|1\rangle_{\mathrm{GB}} \to |0\rangle$ transition due to the static dipole moment $\Delta\boldsymbol{\mu}_{11}$ was ignored in the reasoning because the magnitude of that effect is considerably smaller compared to the discussed effects related to $\Delta\boldsymbol{\mu}_{22}$.

Now let us consider the other edge case: $\Delta\boldsymbol{\mu}_{22} \uparrow\downarrow \boldsymbol{\mathcal{E}}$. The Hamiltonian is now

$$\hat{H}_{\mathrm{S}}^{\uparrow\downarrow} = \begin{pmatrix} 100 & 100 \\ 100 & 0+756 \end{pmatrix}, \tag{88}$$

and the corresponding subsystem parameters are

$$\begin{aligned} &\varepsilon_1^{\uparrow\downarrow} = 76\,\mathrm{cm}^{-1}, \qquad \varepsilon_2^{\uparrow\downarrow} = 760\,\mathrm{cm}^{-1}, \\ &|\boldsymbol{\mu}_{01}^{\uparrow\downarrow}|^2 = 0.98\,\mathrm{D}^2, \quad |\boldsymbol{\mu}_{02}^{\uparrow\downarrow}|^2 = 0.02\,\mathrm{D}^2. \end{aligned} \tag{89}$$

As we can see, the energy of state $|1\rangle_{\mathrm{GB}}$ is again lowered compared to the field-free case, causing a redshift of the fluorescence band. Moreover, in this configuration, we have $\varepsilon_1^{\uparrow\downarrow} < \varepsilon_2^{\uparrow\downarrow}$, leading to the population of state $|1\rangle_{\mathrm{GB}}$ being close to unity, fostering high fluorescence intensity at $\omega = 15076\,\mathrm{cm}^{-1}$. Meanwhile, the dark state shifts to higher frequencies but does not fluoresce there because its population is low and the transition dipole moment is small. Similarly to the previous configuration, the intensity of the dark state band (which is highly fluorescent when no field is present) decreases.

To complete the analysis of Fig. 5a, we turn to an intermediate case where $\Delta\boldsymbol{\mu}_{22}$ is not too far from being perpendicular to $\boldsymbol{\mathcal{E}}$ and set $\vartheta = 105°$. We then have

$$\hat{H}_{\mathrm{S}}^{\vartheta} = \begin{pmatrix} 100 & 100 \\ 100 & 0+196 \end{pmatrix}, \tag{90}$$

and

$$\begin{aligned} &\varepsilon_1^{\vartheta} = 29\,\mathrm{cm}^{-1}, \qquad \varepsilon_2^{\vartheta} = 247\,\mathrm{cm}^{-1}, \\ &|\boldsymbol{\mu}_{01}^{\vartheta}|^2 = 0.72\,\mathrm{D}^2, \quad |\boldsymbol{\mu}_{02}^{\vartheta}|^2 = 0.28\,\mathrm{D}^2. \end{aligned} \tag{91}$$

Here, state $|1\rangle_{\mathrm{GB}}$ ends up being even lower than in the two edge cases analysed before. Its population and transition dipole moment are approximately 3 times greater than the corresponding parameters of state $|2\rangle_{\mathrm{GB}}$, leading to high fluorescence yield. This and the similar configurations contribute to the fluorescence in the region of $\omega \approx 15050\,\mathrm{cm}^{-1}$ in the Stark fluorescence spectrum.

Let us summarise the above analysis and connect it to the resulting Stark fluorescence spectrum in Fig. 5a. The negative band centred at $\omega \approx 14900\,\mathrm{cm}^{-1}$ appears because the external field shifts the energy of state $|2\rangle_{\mathrm{GB}}$, either to the lower frequencies (up to $\omega \approx 14223\,\mathrm{cm}^{-1}$) or to the higher frequencies (up to $\omega \approx 15760\,\mathrm{cm}^{-1}$). However, no noticeable increase of intensity at those frequencies is observed because of the small resulting transition dipole moment of state $|2\rangle_{\mathrm{GB}}$. Next, the negative band centred at $\omega \approx 15150\,\mathrm{cm}^{-1}$ results because the external field lowers the energy of state $|1\rangle_{\mathrm{GB}}$ for most orientations, and the fluorescence band red-shifts. This also contributes to the large intensity maximum positioned at $\omega \approx 15050\,\mathrm{cm}^{-1}$ in the Stark fluorescence spectrum.

Since the Liptay formalism has been developed mainly for Stark absorption experiments [8], the formula (43) becomes inadequate for simulating fluorescence spectra when the equilibrium populations play a major role. As we have just shown, this occurs if one of the states possesses a large static dipole moment and is therefore very sensitive to the external electric field.

Now let us consider a system where the dark state is a CT state which interacts with the environment strongly. The case of $\lambda_2 = 100\,\mathrm{cm}^{-1}$ is illustrated in Fig. 5b. In the fluorescence spectrum, we observe that the lower frequency band, corresponding to the transition from the CT state, is broader than the higher frequency band. This happens precisely because of the strong interaction with the environment. As a result, the left band is calculated less accurately than the right one using the FBTS. In the Stark fluorescence spectrum, these discrepancies translate to an overestimation of the intensity of the positive band, and one may only settle for a qualitative agreement with the exact results. Comparing the shapes of the HEOM spectrum and the F'' curve, we conclude that the latter certainly cannot be used to describe the actual spectrum. This is in part attributed to the fact that the resulting spectrum is distinctly different from all other Stark fluorescence spectra that we have studied so far in this work. Indeed, the absolute values of the minima of the spectrum are equal to approximately 1 unit, while the maximum of intensity reaches 6 units, so the minima are relatively shallow. This effect is even more pronounced in the case of $\lambda_2 = 200\,\mathrm{cm}^{-1}$ shown in Fig. 5c, where the negative part of the Stark fluorescence spectrum to the left of the main band is barely noticeable.

An essential feature of the Stark fluorescence spectra in Fig. 5 is that the integrated intensities are positive rather than being close to zero as in all other cases studied before. This means that the overall fluorescence intensity increases when the system is placed in an external electric field. In the literature, such an increase is attributed exclusively to the decrease of the rate of nonradiative relaxation processes which causes more molecules to relax by emitting a photon [4, 54]. Our simulations, however, do not take into account any nonradiative relaxation channels, therefore, that explanation is inapplicable here.

We argue that the Stark fluorescence spectrum may become mostly positive specifically due to the presence of a CT state, which is most pronounced in Fig. 5c. The Stark fluorescence spectrum shown there may be analysed in the same way as we studied the case in Fig. 5a. The main difference in the present case is that due to the strong coupling with the environment, the CT state does not fluoresce intensely (i.e., its transition dipole moment is small). Hence, when the field is introduced and the energy of the CT state is shifted, the reduction of intensity of the original band is less noticeable. This explains the shallow minimum at $\omega \approx 14800\,\mathrm{cm}^{-1}$ in Fig. 5c. On the other hand, the absence of a minimum at $\omega \approx 15150\,\mathrm{cm}^{-1}$ is supported by the fact that state $|1\rangle_{\mathrm{GB}}$ red-shifts to a lesser extent. Comparing the positions of the maxima of F and F_{S} in Fig. 5c we can see a shift by only approximately $55\,\mathrm{cm}^{-1}$, while in case of $\lambda_2 = 100\,\mathrm{cm}^{-1}$ the shift is by $81\,\mathrm{cm}^{-1}$ (see Fig. 5b), and for $\lambda_2 = 10\,\mathrm{cm}^{-1}$ it is $104\,\mathrm{cm}^{-1}$ (see Fig. 5a).

The relative change η of the overall fluoresce yield may be calculated as the ratio between the integrals of the Stark fluorescence spectrum and the corresponding field-free fluorescence

spectrum:

$$\eta = \frac{\int_{-\infty}^{\infty} F_{\mathrm{S}}(\omega)\,\mathrm{d}\omega}{\int_{-\infty}^{\infty} F(\omega)\,\mathrm{d}\omega}. \tag{92}$$

The values of η calculated from the HEOM data are provided in the corners of the lower plots in Fig. 5. As we can see, the higher the value of λ_2, the more noticeable the increase of intensity is. If the CT state interacts with the bath strongly, $\lambda_2 = 200\,\mathrm{cm}^{-1}$, the intensity increases more than 1.5 times when an external electric field is introduced. For comparison, in the previously studied case of a system with two molecular-excitation states and reorganisation energy $\lambda = 100\,\mathrm{cm}^{-1}$ (Fig. 4b), we obtain $\eta = 10^{-4}$, which is essentially zero at the tolerance level used in our calculations.

We note that the increase of fluorescence yield may be evaluated approximately without performing an actual calculation of the spectrum. It follows from Eq. (37) that the integral of the spectrum is given by the initial value of the dipole–dipole correlation function. If we invoke the approximation (73) at that time moment, just like we did to arrive at Eq. (79), we obtain

$$C_{\mathrm{d-d}}(0) = \mathrm{Tr}_{\mathrm{SB}}\Big((\hat{\boldsymbol{\mu}}\cdot\boldsymbol{\sigma}_E)^2\hat{\rho}_{\mathrm{SB}}(0)\Big) \approx \mathrm{Tr}_{\mathrm{S}}\Big((\hat{\boldsymbol{\mu}}\cdot\boldsymbol{\sigma}_E)^2\hat{\rho}_{\mathrm{S}}(0)\Big), \tag{93}$$

where we used $\mathrm{Tr}_{\mathrm{B}}\big(\hat{\rho}_{\mathrm{B}}(0)\big) = 1$. The subsystem density matrix may be approximated using Eq. (80), and this way $C_{\mathrm{d-d}}(0)$ may be readily obtained. It only remains to perform the orientational averaging, but this step introduces no difficulties. Our calculations have confirmed that the values of η found using Eq. (93) do coincide with those obtained by a direct numerical integration of the calculated HEOM spectra.

2.2.2 Case 2: $\varepsilon_{\mathrm{CT}} > \varepsilon_{\mathrm{bright}}$

The case when the energy of the bright state $|1\rangle$ is lower than that of the CT state $|2\rangle$ is analysed is Fig. 6. The subsystem Hamiltonian in the absence of the field is chosen to be

$$\hat{H}_{\mathrm{S}} = \begin{pmatrix} 0 & 100 \\ 100 & 200 \end{pmatrix}. \tag{94}$$

The first thing we notice in Fig. 6 is that the FBTS is highly accurate in almost all of the demonstrated spectra, with the exception of the Stark fluorescence spectrum in the $\lambda_2 = 200\,\mathrm{cm}^{-1}$ case. Next, we find that the intensity of the right fluorescence band, corresponding to the transition from the CT state, is very weak, and this band is clearly resolved only in the fluorescence spectrum in the $\lambda_2 = 10\,\mathrm{cm}^{-1}$ case. This is natural since the CT state has a small transition dipole moment and its population is also small because its energy is higher than that of the bright state. Speaking of the $\lambda_2 = 10\,\mathrm{cm}^{-1}$ case, we may state that the Stark fluorescence spectrum does resemble the shape of F'', although the agreement is imperfect.

The main effect responsible for the shapes of the depicted Stark fluorescence spectra is the following. The external field may cause the energy of state $|2\rangle_{\mathrm{GB}}$ to become even higher than when there is no field, and as a result of the resonance coupling, the energy of state $|1\rangle_{\mathrm{GB}}$

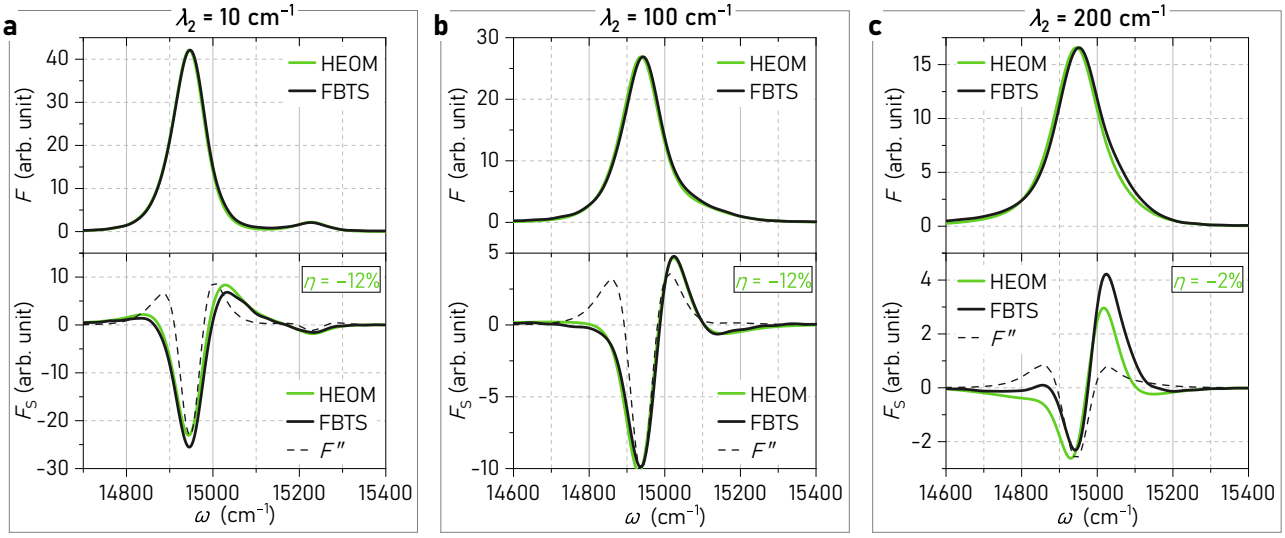

Figure 6: Spectra of systems with one bright state and one CT state, with $\varepsilon_{\mathrm{CT}} > \varepsilon_{\mathrm{bright}}$. Three cases are shown: **(a)** $\lambda_2 = 10\,\mathrm{cm}^{-1}$, **(b)** $\lambda_2 = 100\,\mathrm{cm}^{-1}$, **(c)** $\lambda_2 = 200\,\mathrm{cm}^{-1}$.

becomes higher as well. When the energy of state $|2\rangle_{\mathrm{GB}}$ becomes lower than that of state $|1\rangle_{\mathrm{GB}}$, the energy of the latter again increases. This causes a blueshift of the highly intense fluorescence band at $\omega \approx 14950\,\mathrm{cm}^{-1}$. Consequently, the fluorescence at $\omega \approx 14950\,\mathrm{cm}^{-1}$ becomes less intense, while the fluorescence intensity at $\omega \approx 15050\,\mathrm{cm}^{-1}$ increases, which is illustrated in the Stark fluorescence spectra.

Calculated values of the overall change of the fluorescence intensity are presented in the lower plots of Fig. 6. As we can see, the fluorescence yield decreases in an external field, but if the CT state interacts with the environment very strongly, $\lambda_2 = 200\,\mathrm{cm}^{-1}$, the decrease is hardly noticeable ($\eta = -2\%$). Once again, as we mentioned when studying the case of $\varepsilon_{\mathrm{bright}} > \varepsilon_{\mathrm{CT}}$ in the previous section, an experimentalist's conclusion of such results would be that the nonradiative relaxation processes become more active in the presence of an external field, leading to the decrease of fluorescence yield [3,5,13,54–58]. Our results, however, indicate that the fluorescence yield may decrease due to the presence of a CT state in the system. It is therefore likely that both effects are present in the actual experiments.

2.3 Systems with two molecular-excitation states and one CT state

Now let us study the spectra of slightly more complex systems, consisting of two molecular excitations ($|1\rangle$, $|2\rangle$) and one CT state ($|\mathrm{CT}\rangle \equiv |3\rangle$). In the global basis, we will refer to the state with the smallest transition dipole moment as $|\mathrm{CT}\rangle_{\mathrm{GB}} \equiv |3\rangle_{\mathrm{GB}}$, while the two other states will be called $|1\rangle_{\mathrm{GB}}$ and $|2\rangle_{\mathrm{GB}}$. First, we choose the energy of the CT state to lie lower than those of the other two states, which resembles the case $\varepsilon_{\mathrm{CT}} < \varepsilon_{\mathrm{bright}}$ of Section 2.2.1. The Hamiltonian of the system is the following:

$$\hat{H}_{\mathrm{S}} = \begin{pmatrix} 0 & 50 & 100 \\ 50 & 100 & 100 \\ 100 & 100 & -100 \end{pmatrix}. \tag{95}$$

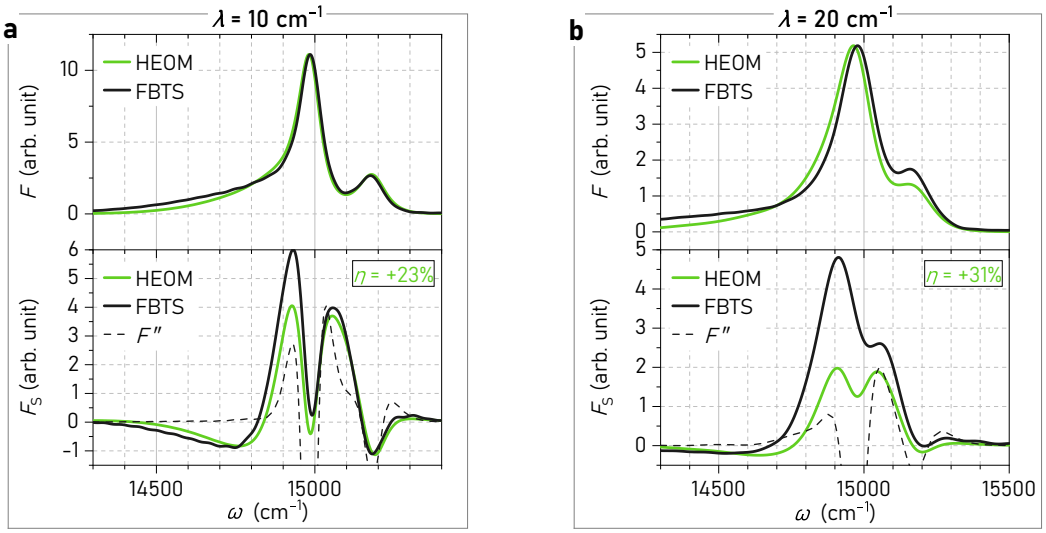

Figure 7: Spectra of systems with two molecular-excitation states and one CT state, with $\varepsilon_{\mathrm{CT}} < \varepsilon_1 < \varepsilon_2$. Two cases are shown: **(a)** $\lambda = 10\,\mathrm{cm}^{-1}$, **(b)** $\lambda = 20\,\mathrm{cm}^{-1}$.

Here and in the following Hamiltonians, the CT state is characterised by the third row and third column. In the present case, the energies of the states are thus (neglecting the $15000\,\mathrm{cm}^{-1}$ bias) $\varepsilon_1 = 0$, $\varepsilon_2 = 100\,\mathrm{cm}^{-1}$, $\varepsilon_{\mathrm{CT}} \equiv \varepsilon_3 = -100\,\mathrm{cm}^{-1}$. The off-diagonal elements of the Hamiltonian represent the couplings between the states: the strength of the coupling between the bright states is $50\,\mathrm{cm}^{-1}$, while the interaction between the bright states and the CT state is twice stronger. The subsystem–bath coupling is specified as follows: we choose a certain base value λ, and the interaction strength for each n-th state is then given by $\lambda_n = \kappa_n \lambda$, where κ_n is a numerical factor. For all of the systems studied in this section, we set $\kappa_1 = \kappa_2 = 1$ and $\kappa_{\mathrm{CT}} \equiv \kappa_3 = 10$.

The spectra calculated using the Hamiltonian in Eq. (95) are studied in Fig. 7. In the field-free fluorescence spectra, we can clearly see two bands corresponding to the bright states. The band corresponding to the CT state, on the other hand, is not directly visible, but it is responsible for the broad tail in the region of lower frequencies. The fluorescence spectra calculated using the FBTS match the HEOM results rather well, although the error is larger in the case of stronger subsystem–bath coupling shown in Fig. 7b. Arguably, that case turns out to be outside of the range of validity of the FBTS if one is interested in the Stark fluorescence spectrum. In the lower part of Fig. 7b, we observe that the FBTS overestimates the intensities of the bands considerably, and their relative intensities are also determined inaccurately. The situation is thus qualitatively the same as in Figs. 5b and 5c, except that here we have two bright states rather than one, and hence two maxima instead of one. The main effect is again that the energies of the bright states become lower in the external electric field due to the coupling with the CT state, and the spectral bands red-shift. Finally, we note that the FBTS remains valid in the regime of weaker subsystem–bath interaction (Figs. 7a), while the Liptay formalism is inapplicable in both cases.

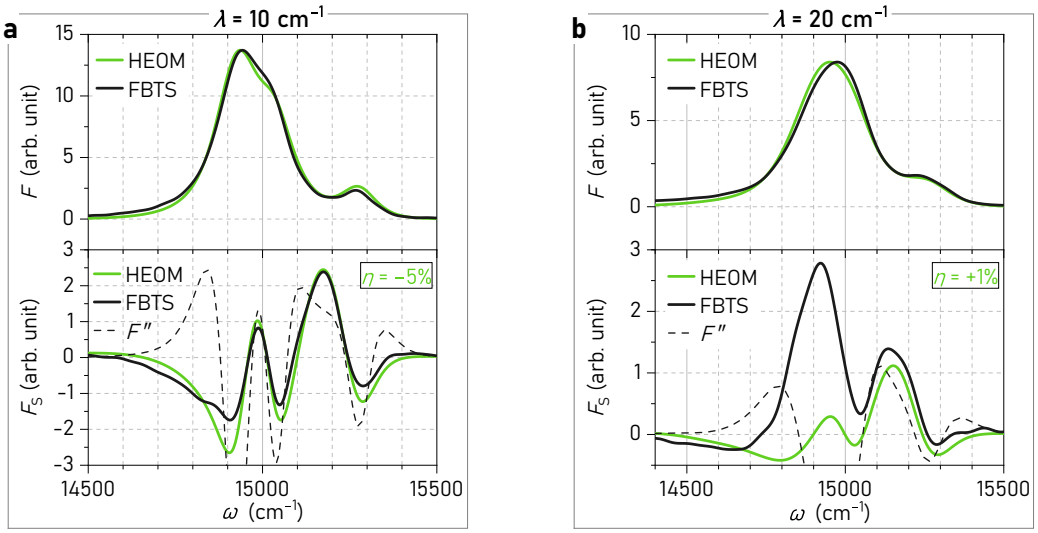

Figure 8: Spectra of systems with two molecular-excitation states and one CT state, with $\varepsilon_1 < \varepsilon_{\mathrm{CT}} < \varepsilon_2$. Two cases are shown: **(a)** $\lambda = 10\,\mathrm{cm}^{-1}$, **(b)** $\lambda = 20\,\mathrm{cm}^{-1}$.

Next, we turn to a subsystem with the Hamiltonian

$$\hat{H}_{\mathrm{S}} = \begin{pmatrix} 0 & 50 & 100 \\ 50 & 200 & 100 \\ 100 & 100 & 100 \end{pmatrix}, \tag{96}$$

where the energies are arranged in such a way so that $\varepsilon_1 < \varepsilon_{\mathrm{CT}} < \varepsilon_2$. Looking closely at the fluorescence spectrum calculated using HEOM in Fig. 8a, we notice that the broad band centred at $\omega \approx 15000\,\mathrm{cm}^{-1}$ is composed of two bands, one of which in fact corresponds to state $|\mathrm{CT}\rangle_{\mathrm{GB}}$. According to the effective coupling theory, those bands should be centred at $\varepsilon_1^{\mathrm{GB}} = -100\,\mathrm{cm}^{-1}$ and $\varepsilon_{\mathrm{CT}}^{\mathrm{GB}} = 27\,\mathrm{cm}^{-1}$, and corresponding the transition dipole moments are $|\boldsymbol{\mu}_{01}^{\mathrm{GB}}|^2 = 0.47\,\mathrm{D}^2$ and $|\boldsymbol{\mu}_{03}^{\mathrm{GB}}|^2 = 0.70\,\mathrm{D}^2$. The CT state thus no longer remains dark in the global basis, and it is responsible for the peak at $\omega \approx 27\,\mathrm{cm}^{-1}$. Consequently, in the Stark fluorescence spectrum in Fig. 8a, we can see three minima corresponding to the three bands of the fluorescence spectrum. The FBTS provides a satisfactory fit of the correct HEOM spectrum, while the F'' curve does not. In Fig. 8b, we can see that the strong coupling again presents difficulties for the FBTS when calculating the Stark fluorescence spectrum. As a result, the quantum-classical method predicts an increase of fluorescence yield by 20%, while the (correct) HEOM result is $\eta = +1\%$.

The final system studied in this section is described by the Hamiltonian

$$\hat{H}_{\mathrm{S}} = \begin{pmatrix} 0 & 50 & 100 \\ 50 & 100 & 100 \\ 100 & 100 & 200 \end{pmatrix}. \tag{97}$$

Here, similarly to the system discussed in Section 2.2.2, the energy of the CT state is the highest in the system: $\varepsilon_{\mathrm{CT}} > \varepsilon_2 > \varepsilon_1$. Comparing the spectra corresponding to the present case (Fig. 9) to those shown in Fig. 6 we notice that they are quite similar. The Stark fluorescence

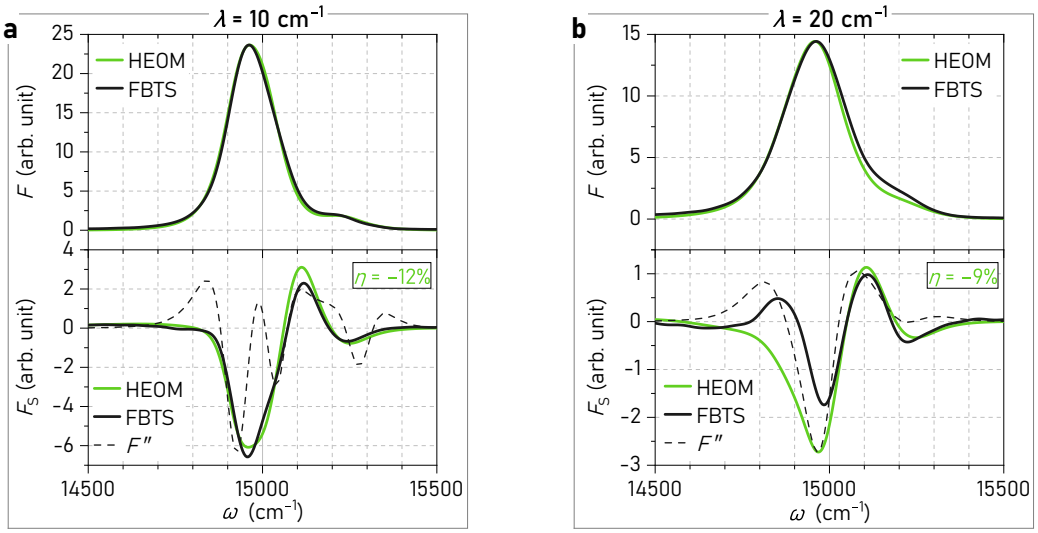

Figure 9: Spectra of systems with two molecular-excitation states and one CT state, with $\varepsilon_{\mathrm{CT}} > \varepsilon_2 > \varepsilon_1$. Two cases are shown: **(a)** $\lambda = 10\,\mathrm{cm}^{-1}$, **(b)** $\lambda = 20\,\mathrm{cm}^{-1}$.

spectra indicate a blueshift of the spectral bands when the field is introduced, and an overall decrease of fluorescence yield takes place. In the upper panel of Fig. 9a, the fluorescence band at $\omega \approx 15000\,\mathrm{cm}^{-1}$ consists of two bands whose maxima are positioned at $\varepsilon_1^{\mathrm{GB}} = -62\,\mathrm{cm}^{-1}$ and $\varepsilon_2^{\mathrm{GB}} = 13\,\mathrm{cm}^{-1}$ according to the effective coupling theory. This explains the corresponding minima of the F'' curve, but the HEOM results indicate that the shape of the correct Stark fluorescence spectrum is a different one. The FBTS results agree with these exact results, but the method once again leads to inaccurate results in the case of stronger subsystem–bath interaction, shown Fig. 9b.

3 Discussion

Let us now summarise the main results of the simulations. In our study we concentrated on three main points: the main features of the Stark fluorescence spectra, the range of validity of the FBTS results, and the applicability of the Liptay formalism. We discuss each aspect separately in the following sections.

3.1 Main features of the Stark fluorescence spectra

The initial part of our analysis has shown that when the static dipole moments of the subsystem are small ($\sim 1.5\,\mathrm{D}$), the shapes of the Stark fluorescence spectra are quite predictable. They largely follow the shapes of the second derivatives of the corresponding field-free fluorescence spectra, allowing for a well-known and a rather straightforward explanation. On the other hand, the presence of states with a large dipole moment ($\sim 15\,\mathrm{D}$) leads to non-trivial results. Analysis of a two-level subsystem where the dipole moments of the states are 1.5 D and 15 D has revealed that an increase or a reduction of total fluorescence yield may be observed when the system is placed in an external electric field. In the Stark fluorescence spectra, this is signified by the integrated intensity being either positive or negative. We argue that this is caused by a change of the average state populations which occurs in an electric field. Let us illustrate this with a calculation for a simplified model.

Consider an ensemble of two-level molecules described by the Hamiltonian

$$\hat{H} = \begin{pmatrix} \varepsilon_1 & 0 \\ 0 & \varepsilon_2 \end{pmatrix}, \tag{98}$$

where the resonant coupling between the states is assumed to be small and is therefore neglected. Let this ensemble interact with a bath of inverse temperature β. According to the canonical distribution, the density matrix of each molecule of the ensemble is

$$\hat{\rho} = \frac{\mathrm{e}^{-\beta\hat{H}}}{\mathrm{Tr}(\mathrm{e}^{-\beta\hat{H}})} = \begin{pmatrix} \dfrac{1}{1+\mathrm{e}^{\beta\Delta}} & 0 \\ 0 & \dfrac{1}{1+\mathrm{e}^{-\beta\Delta}} \end{pmatrix}, \quad \Delta \equiv \varepsilon_1 - \varepsilon_2. \tag{99}$$

When an external electric field is turned on, the Hamiltonian of each molecule becomes

$$\hat{H}^{\mathcal{E}}(\vartheta,\phi) = \begin{pmatrix} \varepsilon_1 - \boldsymbol{\mu}_{11}\cdot\boldsymbol{\mathcal{E}} & 0 \\ 0 & \varepsilon_2 - \boldsymbol{\mu}_{22}\cdot\boldsymbol{\mathcal{E}} \end{pmatrix}, \tag{100}$$

where $\boldsymbol{\mu}_{11}$ and $\boldsymbol{\mu}_{22}$ are the static dipole moments of the states. The density matrices of the molecules will then depend on the orientation:

$$\hat{\rho}^{\mathcal{E}}(\vartheta,\phi) = \begin{pmatrix} \dfrac{1}{1+\mathrm{e}^{\beta(\Delta-\boldsymbol{\mu}\cdot\boldsymbol{\mathcal{E}})}} & 0 \\ 0 & \dfrac{1}{1+\mathrm{e}^{-\beta(\Delta+\boldsymbol{\mu}\cdot\boldsymbol{\mathcal{E}})}} \end{pmatrix}, \quad \boldsymbol{\mu} \equiv \boldsymbol{\mu}_{11} - \boldsymbol{\mu}_{22}. \tag{101}$$

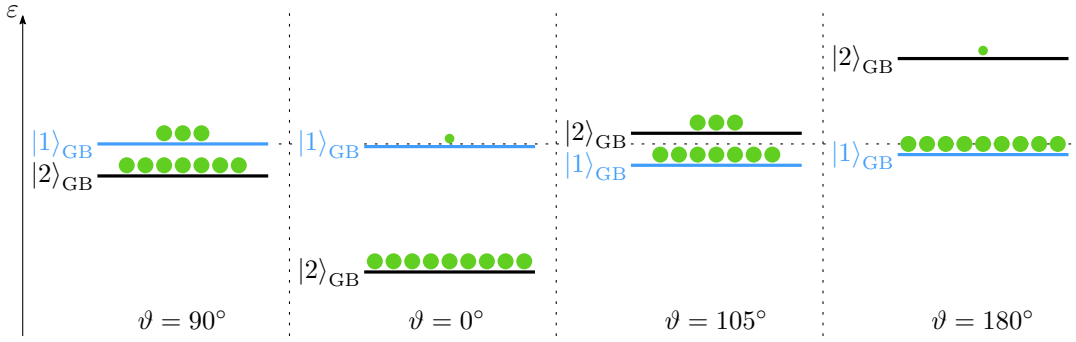

Figure 10: Schematic representation of the subsystem energy levels for different angles ϑ between $\boldsymbol{\mu}$ and $\boldsymbol{\mathcal{E}}$. The green circles represent level populations, and a small circle indicates $\sim 3\%$ of the total population. The figure is drawn to scale — the sizes of the energy gaps and the relative level populations illustrate the calculations of Section 2.2.1, Eqs. (85)–(91).

The aim is now to compare the average population of state $|1\rangle$ with and without the field. The orientationally-averaged population of state $|1\rangle$ with the field on is

$$\left\langle \rho_{11}^{\mathcal{E}} \right\rangle_{\text{or}} = \frac{1}{4\pi} \int_0^{2\pi} \mathrm{d}\phi \int_0^{\pi} \mathrm{d}\vartheta \, \sin\vartheta \, \frac{1}{1 + \mathrm{e}^{\beta(\Delta - \mu\mathcal{E}\cos\vartheta)}} = 1 - \frac{1}{2\beta\mu\mathcal{E}} \ln \frac{1 + \mathrm{e}^{\beta(\Delta+\mu\mathcal{E})}}{1 + \mathrm{e}^{\beta(\Delta-\mu\mathcal{E})}}. \tag{102}$$

As we can see, generally, the external field changes the average population: $\left\langle \rho_{11}^{\mathcal{E}} \right\rangle_{\text{or}} \neq \rho_{11}$. Specifically, we have

$$\begin{cases} \left\langle \rho_{11}^{\mathcal{E}} \right\rangle_{\text{or}} > \rho_{11} & \text{if } \Delta > 0, \\ \left\langle \rho_{11}^{\mathcal{E}} \right\rangle_{\text{or}} < \rho_{11} & \text{if } \Delta < 0, \\ \left\langle \rho_{11}^{\mathcal{E}} \right\rangle_{\text{or}} = \rho_{11} & \text{if } \Delta = 0. \end{cases} \tag{103}$$

Thus, the average population of the level that is higher (when no field is present) increases in the external field, and the average population of the lower one decreases. The process is illustrated in Fig. 10, which corresponds to the situations calculated in Section 2.2.1, Eqs. (85)–(91). The populations of the levels are proportional to the number of green circles (a small circle indicates $\sim 3\%$ of the total population), and ϑ is the angle between $\boldsymbol{\mu}$ and $\boldsymbol{\mathcal{E}}$. The leftmost part corresponds to the situation when no external field is present or when $\boldsymbol{\mu} \perp \boldsymbol{\mathcal{E}}$. When the orientation of the field is such that $\vartheta < 90°$, the population of the higher level reduces, but not by a substantial amount since it is small even without the field. In the depicted edge case when $\vartheta = 0$, the decrease of population is by $\sim 90\%$. On the contrary, when the orientation is such that $\vartheta > 90°$, the population of the level that was initially higher increases noticeably — by $\sim 200\%$ when $\vartheta = 180°$. As the calculation above has shown, on average, an increase of population takes place. If we now choose state $|2\rangle$ to be dark, then an overall increase of fluorescence yield will be observed in an external field because there will be more molecules in the bright states $|1\rangle$ compared to the field-free situation.

In Fig. 10, it is assumed that the static dipole moments of the states are different and the static dipole moment of state $|2\rangle$ (and hence of $|2\rangle_{\text{GB}}$ as well) is greater, corresponding to the case studied in Section 2.2.1. We have also illustrated that the energy of state $|1\rangle_{\text{GB}}$ depends

on the orientation, even if its static dipole moment is zero — this is supported by the direct calculations performed in Section 2.2.1. The exact energies of the states therefore depend on the orientation and the specific values of $\boldsymbol{\mu}_{11}$ and $\boldsymbol{\mu}_{22}$. On the other hand, as far as the average populations are concerned, only the magnitude of the difference vector $\boldsymbol{\mu}$ is important (for this illustratory system, at least), which is clearly seen in Eq. (102).

Finally, let us evaluate the magnitude of the possible increase of the average population of the higher level. Choosing parameters similar to those used in Section 2.2.1,

$$\varepsilon_1 = 100\,\mathrm{cm}^{-1}, \quad \varepsilon_2 = 0, \quad T = 300\,\mathrm{K}, \quad E = 3\,\mathrm{MV/cm}, \quad \mu = 15\,\mathrm{D}. \tag{104}$$

we find

$$\rho_{11} = 0.38, \quad \rho_{11}^{\mathcal{E}} = 0.44, \tag{105}$$

which yields a 14% increase of the average population of the bright state. Meanwhile, we obtained an increase of the fluorescence yield $\eta = +13\%$ in Section 2.2.1 when the subsystem–bath coupling was small (see Fig. 5a). Obviously, the similarity of these results is mostly accidental since we neglected the coupling between the states in the present calculation. Moreover, additional orientational effects arising from the terms $\hat{\boldsymbol{\mu}} \cdot \boldsymbol{\sigma}_E$ in the dipole–dipole correlation function (31) are important for the calculation of spectra. Nevertheless, the calculation of the average populations preformed here provides an explanation of this effect, and it also explains the growth of the value of η for higher reorganisation energies that was observed in Section 2.2.1 (see Fig. 5). Indeed, according to the effective coupling theory, if the reorganisation energies of the states are different, then the energy gap between them increases (note the $-\hat{\Lambda}$ term in Eq. (81)), and it follows from Eqs. (99) and (102) that the relative increase of population, $\left(\left\langle \rho_{11}^{\mathcal{E}} \right\rangle_{\mathrm{or}} - \rho_{11}\right)/\rho_{11}$, grows monotonically with increasing energy gap Δ. For clarity, we note that the reduction of the fluorescence yield that we found in Section 2.2.2 (see Fig. 6) is caused by the fact that there, the bright state is lower than the dark one, and the orientationally-averaged population of the lower state reduces in an external field (see Eq. (103)).

The simulations of the three-level subsystems that we performed in Section 2.3 have demonstrated that the resulting Stark fluorescence spectra may be interpreted similarly to those corresponding to the two-level systems. When the CT state, possessing a large static dipole moment, was the lowest state in the system, a total increase of fluorescence yield in an external field was observed. When the energy of the CT state was in the middle of the energies of the two other states, we have seen a reduction of fluorescence intensity for smaller values of λ and an increase for higher values. Systems where the CT state is the highest indicate that the fluorescence intensity decreases when an external electric field is introduced.

3.2 Range of validity of the FBTS results

Reviewing the accuracy of the spectra calculated using the FBTS, we may notice several trends although generally the dependence of the accuracy on the parameters is non-trivial. First, all of the calculated field-free fluorescence spectra provide quantitatively correct results and may

be used for fitting experimental data. On the other hand, the Stark fluorescence spectra are calculated less accurately in almost all of the studied cases — even the smallest discrepancies seen in the field-free spectra seem to be amplified in the corresponding Stark spectra. Next, the accuracy almost certainly falls down with increasing subsystem–bath coupling strength. If at least one of the subsystem states interacts with the environment strongly ($\lambda \sim 100\,\mathrm{cm}^{-1}$), one should not expect the calculated Stark fluorescence spectrum to be quantitatively correct. The results in Fig. 6b, however, present an exception as the FBTS Stark spectrum matches the exact HEOM curves almost perfectly in that case. Turning to the three-level subsystems, we notice that very strong interaction with the environment ($\lambda \sim 200\,\mathrm{cm}^{-1}$) might lead to the FBTS results being wrong even at the qualitative level.

Thus, we are lead to conclude that the FBTS may prove useful for simulating and perhaps analysing the experimental data of the field-free fluorescence spectra. The FBTS may also be used to get an estimate of the shape of the Stark fluorescence spectrum if the model of the subsystem assumes moderate strength of coupling with the bath ($\lambda \lesssim 100\,\mathrm{cm}^{-1}$).

3.3 Applicability of the Liptay formalism

Application of the Liptay formalism for the Stark fluorescence spectra simulated in this work has revealed that the second derivative curve provides a reasonable approximation of the exact results only when there are no CT states in the system. Even if a band corresponding to a CT state is clearly visible in the field-free fluorescence spectrum, it does not simply broaden when the fields is applied, but causes a shift of other bands and a change in the fluorescence yield as discussed in Section 3.1. These effects are not encoded in the shapes of the field-free spectra and therefore cannot be represented correctly by the second derivative curves.

At this point, it might appear that we should have tried fitting the spectra using all three terms of the Liptay formula (43) instead of using only the last one. While it is likely that we would have been able to get a very good agreement with the exact results that way, the interpretation of the fitted coefficient would be questionable. For example, the inclusion of the first derivative component would certainly provide a better fit in cases when the band shift is observed, but the obtained coefficient B_χ would indicate that some of the elements of the polarisability tensor are non-zero, which does not correspond to the actual model that we used. It is, however, possible that the Liptay formula (43) may nonetheless be useful if the expressions for the coefficients are adapted to account for the effects caused by the CT states.

Conclusions

1. The presence of charge-transfer states in the system may cause a change of the total fluorescence yield in an external electric field: an increase if the energy of this state is the lowest in the system, or a reduction if its energy is the highest among all states.

2. The quantum-classical FBTS method may be applied for simulating the Stark fluorescence spectra if the subsystem–bath coupling strength does not exceed the strength of the resonance coupling ($\lambda/J \lesssim 1$).

3. The Liptay formalism does not allow for an estimation of the magnitude of the specific effects caused by the presence of charge-transfer states in the system.

Acknowledgements

Computations were performed on resources at the supercomputer 'VU HPC' of Vilnius University in the Faculty of Physics location.

References

[1] W. Demtröder, *Laser Spectroscopy 1.* Springer Berlin Heidelberg, 2014.

[2] R. N. Frese, M. Germano, F. L. de Weerd, *et al.*, Electric field effects on the chlorophylls, pheophytins, and β-carotenes in the reaction center of Photosystem II, *Biochemistry*, 2003, **42**, 9205–9213.

[3] M. Wahadoszamen, T. Nakabayashi, S. Kang, H. Imahori, and N. Ohta, External electric field effects on absorption and fluorescence spectra of a fullerene derivative and its mixture with zinc-tetraphenylporphyrin doped in a PMMA film, *J. Phys. Chem. B*, 2006, **110**, 20354–20361.

[4] M. Wahadoszamen, T. Hamada, T. Iimori, T. Nakabayashi, and N. Ohta, External electric field effects on absorption, fluorescence, and phosphorescence spectra of diphenylpolyynes in a polymer film, *J. Phys. Chem. A*, 2007, **111**, 9544–9552.

[5] M. Wahadoszamen, E. Belgio, M. A. Rahman, A. M. Ara, A. V. Ruban, and R. van Grondelle, Identification and characterization of multiple emissive species in aggregated minor antenna complexes, *Biochim. Biophys. Acta*, 2016, **1857**, 1917–1924.

[6] A. M. Ara, M. S. B. Kashem, R. van Grondelle, and M. Wahadoszamen, Stark fluorescence spectroscopy on peridinin–chlorophyll–protein complex of dinoflagellate, *Amphidinium carterae*, *Photosynth. Res.*, 2019, **143**, 233–239.

[7] A. Loukianov, A. Niedringhaus, B. Berg, J. Pan, S. S. Senlik, and J. P. Ogilvie, Two-dimensional electronic Stark spectroscopy, *J. Phys. Chem. Lett.*, 2017, **8**, 679–683.

[8] W. Liptay, Dipole moments and polarizabilities of molecules in excited electronic states, in *Excited States* (E. C. Lim, ed.), vol. 1, 129–229, Elsevier, 1974.

[9] G. U. Bublitz and S. G. Boxer, Stark spectroscopy: Applications in chemistry, biology, and materials science, *Annu. Rev. Phys. Chem.*, 1997, **48**, 213–242.

[10] S. G. Boxer, Stark realities, *J. Phys. Chem. B*, 2009, **113**, 2972–2983.

[11] V. May and O. Kühn, *Charge and Energy Transfer Dynamics in Molecular Systems.* Wiley VCH Verlag GmbH, 2011.

[12] R. E. Blankenship, *Molecular Mechanisms of Photosynthesis.* Chichester: Wiley Blackwell, 2014.

[13] M. Wahadoszamen, I. Margalit, A. M. Ara, R. van Grondelle, and D. Noy, The role of charge-transfer states in energy transfer and dissipation within natural and artificial bacteriochlorophyll proteins, *Nat. Commun.*, 2014, **5**.

[14] D. S. Gottfried, J. W. Stocker, and S. G. Boxer, Stark effect spectroscopy of bacteriochlorophyll in light-harvesting complexes from photosynthetic bacteria, *Biochim. Biophys. Acta*, 1991, **1059**, 63–75.

[15] O. J. G. Somsen, V. Chernyak, R. N. Frese, R. van Grondelle, and S. Mukamel, Excitonic interactions and Stark spectroscopy of light harvesting systems, *J. Phys. Chem. B*, 1998, **102**, 8893–8908.

[16] H. van Amerongen, L. Valkunas, and R. van Grondelle, *Photosynthetic Excitons*. World Scientific, 2000.

[17] A. Gelzinis, D. Abramavicius, J. P. Ogilvie, and L. Valkunas, Spectroscopic properties of Photosystem II reaction center revisited, *J. Chem. Phys.*, 2017, **147**, 115102.

[18] A. Gelzinis, L. Valkunas, F. D. Fuller, J. P. Ogilvie, S. Mukamel, and D. Abramavicius, Tight-binding model of the Photosystem II reaction center: Application to two-dimensional electronic spectroscopy, *New J. Phys.*, 2013, **15**, 075013.

[19] E. G. Lewars, *Computational Chemistry*. Springer International Publishing, 2016.

[20] S. M. Bachrach, *Computational Organic Chemistry*. WILEY, 2014.

[21] H.-P. Breuer and F. Petruccione, *The theory of open quantum systems*. Oxford New York: Oxford University Press, 2002.

[22] V. I. Novoderezhkin, M. A. Palacios, H. van Amerongen, and R. van Grondelle, Energy-transfer dynamics in the LHCII complex of higher plants: Modified Redfield approach, *J. Phys. Chem. B*, 2004, **108**, 10363–10375.

[23] T. Renger, Theory of excitation energy transfer: From structure to function, *Photosynth. Res.*, 2009, **102**, 471–485.

[24] T. Renger, M. Madjet, A. Knorr, and F. Müh, How the molecular structure determines the flow of excitation energy in plant light-harvesting complex II, *J. Plant Physiol.*, 2011, **168**, 1497–1509.

[25] L. Chen, R. Zheng, Y. Jing, and Q. Shi, Simulation of the two-dimensional electronic spectra of the Fenna-Matthews-Olson complex using the hierarchical equations of motion method, *J. Chem. Phys.*, 2011, **134**, 194508.

[26] D. Abramavicius and S. Mukamel, Energy-transfer and charge-separation pathways in the reaction center of Photosystem II revealed by coherent two-dimensional optical spectroscopy, *J. Chem. Phys.*, 2010, **133**, 184501.

[27] S. Mukamel, *Principles of Nonlinear Optical Spectroscopy*. Oxford University Press, 1999.

[28] D. P. Craig and T. Thirunamachandran, *Molecular Quantum Electrodynamics*. Dover Publications Inc., 1998.

[29] J. D. Cresser, Theory of the spectrum of the quantised light field, *Physics Reports*, 1983, **94**, 47–110.

[30] L. D. Landau and E. M. Lifshitz, *Quantum Mechanics: Non-Relativistic Theory*, vol. 3 of *Course of Theoretical Physics*. Butterworth-Heinemann, 1981.

[31] L. D. Landau and E. M. Lifshitz, *Quantum Electrodynamics*, vol. 4 of *Course of Theoretical Physics*. Butterworth-Heinemann, 1982.

[32] R. Loudon, *The quantum theory of light*. Oxford New York: Oxford University Press, 2000.

[33] Y. Braver, L. Valkunas, and A. Gelzinis, Derivation of the stationary fluorescence spectrum formula for molecular systems from the perspective of quantum electrodynamics, *Lith. J. Phys.*, (in press).

[34] S. S. Andrews, Using rotational averaging to calculate the bulk response of isotropic and anisotropic samples from molecular parameters, *J. Chem. Educ.*, 2004, **81**, 877.

[35] L. D. Landau and E. M. Lifshitz, *Mechanics*, vol. 1 of *Course of Theoretical Physics*. Butterworth-Heinemann, 1976.

[36] Y. Jing, L. Chen, S. Bai, and Q. Shi, Equilibrium excited state and emission spectra of molecular aggregates from the hierarchical equations of motion approach, *J. Chem. Phys.*, 2013, **138**, 045101.

[37] J. M. Moix, J. Ma, and J. Cao, Förster resonance energy transfer, absorption and emission spectra in multichromophoric systems. III. Exact stochastic path integral evaluation, *J. Chem. Phys.*, 2015, **142**, 094108.

[38] D. I. Blokhintsev, *Quantum Mechanics*. Springer Netherlands, 1964.

[39] W. Liptay, Electrochromism and solvatochromism, *Angew. Chem. Int. Ed.*, 1969, **8**, 177–188.

[40] R. J. Glauber, Coherent and incoherent states of the radiation field, *Phys. Rev.*, 1963, **131**, 2766–2788.

[41] G. Bel and F. L. H. Brown, Theory of single molecule emission spectroscopy, *J. Chem. Phys.*, 2015, **142**, 174104.

[42] B. R. Mollow, Pure-state analysis of resonant light scattering: Radiative damping, saturation, and multiphoton effects, *Phys. Rev. A*, 1975, **12**, 1919–1943.

[43] P. Kumar and S. Jang, Emission lineshapes of the B850 band of light-harvesting 2 (LH2) complex in purple bacteria: A second order time-nonlocal quantum master equation approach, *J. Chem. Phys.*, 2013, **138**, 135101.

[44] R. Kapral, Quantum dynamics in open quantum-classical systems, *J. Phys.: Condens. Matter*, 2015, **27**, 073201.

[45] L. D. Landau and E. M. Lifshitz, *Statistical Physics, Part 1*, vol. 5 of *Course of Theoretical Physics*. Butterworth-Heinemann, 1981.

[46] C.-Y. Hsieh and R. Kapral, Nonadiabatic dynamics in open quantum-classical systems: Forward-backward trajectory solution, *J. Chem. Phys.*, 2012, **137**, 22A507.

[47] G. Stock and M. Thoss, Semiclassical description of nonadiabatic quantum dynamics, *Phys. Rev. Lett.*, 1997, **78**, 578–581.

[48] M. Thoss and G. Stock, Mapping approach to the semiclassical description of nonadiabatic quantum dynamics, *Phys. Rev. A*, 1999, **59**, 64–79.

[49] G. Stock and M. Thoss, Classical description of nonadiabatic quantum dynamics, in *Advances in Chemical Physics*, 243–375, John Wiley & Sons, Inc., 2005.

[50] Y. Braver, L. Valkunas, and A. Gelzinis, Benchmarking the forward–backward trajectory solution of the quantum-classical Liouville equation, *J. Chem. Phys.*, 2020, **152**, 214116.

[51] Y. Braver, Application of quantum-classical Liouville equation for simulation of electronic excitation dynamics, Bachelor's final thesis, Vilnius University, 2019.

[52] J.-J. Ding, J. Xu, J. Hu, R.-X. Xu, and Y. Yan, Optimized hierarchical equations of motion theory for Drude dissipation and efficient implementation to nonlinear spectroscopies, *J. Chem. Phys.*, 2011, **135**, 164107.

[53] A. Gelzinis and L. Valkunas, Analytical derivation of equilibrium state for open quantum system, *J. Chem. Phys.*, 2020, **152**, 051103.

[54] N. Ohta, Electric field effects on photochemical dynamics in solid films, *Bull. Chem. Soc. Jpn.*, 2002, **75**, 1637–1655.

[55] N. Ohta, M. Koizumi, S. Umeuchi, Y. Nishimura, and I. Yamazaki, External electric field effects on fluorescence in an electron donor and acceptor system: Ethylcarbazole and dimethyl terephthalate in PMMA polymer films, *J. Phys. Chem.*, 1996, **100**, 16466–16471.

[56] T. Nakabayashi, M. Wahadoszamen, and N. Ohta, External electric field effects on state energy and photoexcitation dynamics of diphenylpolyenes, *J. Am. Chem. Soc.*, 2005, **127**, 7041–7052.

[57] M. Wahadoszamen, R. Berera, A. M. Ara, E. Romero, and R. van Grondelle, Identification of two emitting sites in the dissipative state of the major light harvesting antenna, *Phys. Chem. Chem. Phys.*, 2012, **14**, 759–766.

[58] M. Wahadoszamen, A. Ghazaryan, H. E. Cingil, A. M. Ara, C. Büchel, R. van Grondelle, and R. Berera, Stark fluorescence spectroscopy reveals two emitting sites in the dissipative state of FCP antennas, *Biochim. Biophys. Acta*, 2014, **1837**, 193–200.

Jakov Braver

Molekulinių sistemų fluorescencijos Štarko spektrų modeliavimas

Santrauka

Optinė spektroskopija yra pagrindinis molekulinių sistemų tyrimo būdas. Ypač informatyvūs yra Štarko spektroskopijos eksperimentai, leidžiantys nustatyti sistemos elektrinius dipolinius momentus ir poliarizuojamumus. Fluorescencijos (ir, analogiškai, sugerties) Štarko spektras apibrėžiamas kaip dviejų spektrų skirtumas: išmatuoto esant išoriniam statiniam elektriniam laukui ir be jo. Šie skirtuminiai spektrai padeda charakterizuoti dideliu statiniu elektriniu dipoliniu momentu pasižyminčias tamsines krūvio pernašos (CT) būsenas, atliekančias svarbų vaidmenį fotosintezės procese.

Eksperimentinių duomenų interpretacija yra sudėtingas uždavinys, nes registruojamą spektrą neišvengiamai lemia daug įvairių fizikinių efektų ir sistemoje vykstančių procesų. Štarko spektroskopinių duomenų analizei plačiai naudojamas Liptay formalizmas, kuris dėka savo paprastumo tapo pagrindiniu ir, faktiškai, vieninteliu analizės būdu, taikomu šioje srityje. Tačiau keliuose darbuose buvo pastebėta, kad naudojantis šiuo analizės būdu gaunamos nefizikinės sistemos parametrų reikšmės. Buvo pradėta kurti naujas Štarko spektrų analizės metodikas, tačiau kol kas jos apsiriboja tik paprastesniais – sugerties – Štarko spektrais. Iki šiol literatūroje nėra paskelbta fluorescencijos Štarko spektrų modeliavimo metodikų, paremtų mikroskopiniu aprašymu, – esamas darbas yra pirmasis žingsnis šia linkme.

Šio darbo tikslas yra sumodeliuoti fluorescencijos Štarko spektrus ir išsiaiškinti, kokią įtaką spektrų formai turi sistemoje esančios CT būsenos. Modeliavimo metu tikrinama, ar Liptay formalizmo rezultatai sutampa su gaunamais kitu, formaliai tiksliu metodu. Taip pat siekiama pritaikyti fluorescencijos Štarko spektrų skaičiavimui kvantine-klasikine teorija paremtą metodą, kuris galėtų būti naudojamas tais atvejais, kai formaliai tikslus skaičiavimas nėra įmanomas.

Skaičiavimams atlikti taikoma atviruųjų kvantinių sistemų teorija: molekulinė sistema skirstoma į elektroninių lygmenų posistemę ir virpesinę aplinką. Spontaninis spinduliavimas aprašomas naudojantis kvantinės elektrodinamikos principais, o fluorescencijos Štarko spektras skaičiuojamas kaip dipolių koreliacinės funkcijos Furjė vaizdas. Formaliai tikslūs rezultatai gaunami Hierarchinių judėjimo lygčių (HEOM) metodu, tačiau jis pasižymi keliais trukumais: jis tinka tik siaurai modelių klasei ir netinka didelių sistemų modeliavimui dėl per didelio kiekio reikalingų skaičiavimo resursų. Šių trūkumų pavyksta išvengti pritaikius kvantine-klasikine teorija paremtą Tiesioginių ir atgalinių trajektorijų sprendinio (FBTS) metodą.

Pirmame šio darbo etape modeliuojamos sistemos, sudarytos iš dviejų sužadintų elektroninių būsenų, kurios abi yra šviesinės. Varijuojant sistemos parametrus, nustatoma, kad daugumoje atvejų FBTS metodas leidžia kiekybiškai teisingai suskaičiuoti šių sistemų tiek įprastus fluorescencijos, tiek fluorescencijos Štarko spektrus. Detalizuojant, FBTS tikslumas krenta stiprėjant posistemės sąveikos su aplinka stipriui, didėjant energijos tarpui tarp lygmenų bei esant silpnai sąveikai tarp jų. Liptay formulės tikslumas yra panašus.

Antrame etape nagrinėjamos sistemos, kuriose viena būsena yra šviesinė, o kita – tamsinė CT būsena. Šiuo atveju fluorescencijos Štarko spektruose stebima, kad suminis fluorescencijos intensyvumas padidėja esant išoriniam elektriniam laukui, jeigu CT būsenos energija yra mažesnė nei šviesinės būsenos (kai išorinio lauko nėra). Priešingu atveju stebimas suminio fluorescencijos intensyvumo sumažėjimas įjungus išorinį lauką. Taip pat rezultatai nurodo, kad Liptay formulė yra praktiškai netinkama šiais atvejais, kadangi jos pagalba suskaičiuoti spektrai net kokybiškai nesutampa su HEOM rezultatais. Tuo tarpu kvantinis-klasikinis FBTS metodas yra kokybiškai teisingas, nors tikslumas yra nepatenkinamas tais atvejais, kai CT būsenos sąveikos su aplinka stipris yra labai didelis.

Trečiame etape sistemos papildomos dar viena šviesine būsena, taigi iš viso sistemoje yra dvi šviesinės būsenos ir viena CT būsena. Fluorescencijos Štarko spektruose vėl stebimas suminio fluorescencijos intensyvumo padidėjimas arba sumažėjimas priklausomai nuo būsenų energijų konfigūracijos. Nustatoma, kad Liptay formulė yra netinkama nė vienu išnagrinėtu atveju, o FBTS metodas tinka tik kai CT būsenos sąveikos su aplinka stipris yra vidutinio stiprumo, bet net ir tais atvejais kiekybinis tikslumas nėra užtikrinamas.

Paskutinėje darbo dalyje analiziškai išnagrinėjama dviejų lygmenų sistema esant išoriniam elektriniam laukui. Pasirinkus supaprastintą sistemą, kurioje sąveikos tarp lygmenų galima nepaisyti, suskaičiuojamos vidutinės lygmenų užpildos, suvirdurkinant per būsenų statinio dipolinio momento ir išorinio elektrinio lauko tarpusavio orientacijas. Šie skaičiavimai rodo, kad aukštesnės energijos lygmens užpilda padidėja išoriniame elektriniame lauke lyginant su atveju, kai lauko nėra. Atitinkamai, vidutinė žemesnio lygmens užpilda sumažėja išoriniame lauke. Taip paaiškinami fluorescencijos Štarko spektruose stebimi suminio intensyvumo padidėjimai arba sumažėjimai.

Darbo pabaigoje suformuluojamos šios išvados:

1. Krūvio pernašos būsenų buvimas sistemoje gali sukelti suminio fluorescencijos intensyvumo pokytį išoriniame elektriniame lauke: padidėjimą, jei šios būsenos energija mažesnė nei kitų būsenų energijos, arba sumažėjimą, jei jos energija didesnė nei kitų būsenų.

2. Kvantinis-klasikinis FBTS metodas gali būti taikomas fluorescencijos Štarko spektrų modeliavimui, jeigu posistemės sąveikos su aplinka stipris neviršija rezonansinės sąveikos stiprio ($\lambda/J \lesssim 1$).

3. Liptay formalizmas neleidžia nustatyti krūvio pernašos būsenų sukeltų efektų didumo.